Performance of long-path optical-microwave Scintillometry

Moonen, R.P.J (Author)

dr. ir. Hartogensis, O.K. (Supervisor)

Wageningen University and Research

March 2021

Abstract

LAS-MWS scintillometry is a technique designed to determine area averaged sensible (H) and latent heat (LvE) fluxes in the atmospheric surface layer at high temporal resolutions. We validated this method at the near homogeneous CESAR cite (NL) by using Eddy Covariance (EC), lysimeter, and surface energy balance data. To gain additional understanding of scintillometry we performed 'virtual' scintillometer and surface flux measurements in a LES which simulated the CESAR site. We developed a new 'dew detecting' method to tackle sign ambiguity in scintillometry and countered MOST non-universality by performing several MOST optimizations. In addition, we investigated the impact of entrainment by using the skewness of q and quadrant analysis of LvE as tracers. The dew detecting method was more similar to EC then the Hill, Lüdi, and Hybrid methods, with a $R^2_{1:1}$ of 0.84 in terms of H and 0.84 in terms of LvE. Scintillometry overestimated LvE due to MOST violations during entrainment events linked to the development and destruction of the CBL. Furthermore, we observed significant under closure of the surface energy balance, also in the LES. Similarity between actual and 'virtual' scintillometry was large, except for some environmental details not resolved in the LES. Our research suggests that during unstable conditions, LAS-MWS scintillometry is a robust tool for determining H and LvE, where precise determination of LvE is limited by weather dependence of MOST. While we improved reliability during stable conditions, convergence issues, noise induced positive r_{Tq}'s, and disconnection from the surface layer seriously hampered the ability of our scintillometer to reliably resolve the turbulent fluxes.

Contents

1 Introduction

Determining the surface fluxes of heat (H) and moisture (LvE) within the convective boundary layer (CBL) has proven difficult due to the chaotic nature and wide range of spatial and temporal scales involved in the turbulent transport process (George, 2010; Xin et al., 2001)[1]. However, we do need measurements of these fluxes since they are essential for many hydro-meteorological applications such as: Flood warning systems that need to know the evapotranspiration in their catchments (Samain et al., 2011) and numerical weather prediction models or remote sensing techniques that must be validated and parameterized. (Beyrich et al., 2002; Brunsell et al., 2011; Samain et al., 2012). One direct and effective method to determine these fluxes is Eddy Covariance (EC). It measures the H and LvE fluxes by sampling the vertical wind speed (w), the temperature (T) and the humidity (q) at high frequencies ($10 - 50Hz$). The calculated covariance between the timeseries of w and T ($\overline{w'T'}$) and w and q ($\overline{w'q'}$) can subsequently be related to the fluxes of H and LvE respectively. Although EC is the normative technique in surface layer meteorology, it has considerable limitations:

- EC is unable to resolve fluxes at temporal resolutions higher then 10 minutes. (Vilà-Guerau De Arellano et al., 2020).
- EC has a rather small and variable footprint. (Foken, 2008).
- Averaging in time instead of in space leads to improper measurement of the field scale fluxes (Kanda et al., 2004).
- EC-stations tend to underestimate the actual vertical wind speed (Kochendorfer et al., 2012).
- The energy balance closure problem that has been linked to underestimation of H and LvE by EC systems (Foken, 2008; Schalkwijk et al., 2015).

Clearly, an additional measurement method which compliments the EC method's weaknesses would be welcome.

Scintillometry is a promising technique which is hoped to fulfil exactly that complementary function (Ward, 2017). Its measurement principle is based on refraction which occurs when electromagnetic radiation encounters a medium shift at an angle, which causes the ray to change direction (this is the principle that causes the mismatch between our perceived understanding of where a fish is under a water surface and where it actually is). Since - for a set wavelength (λ) - the refractive index of air is dependent on its q and T, a ray that travels through the turbulent atmospheric surface layer (ASL) gets refracted by the transitions between turbulent eddies of various T's and q's. A scintillometer capitalizes on this effect by sending a monochromatic beam from a transmitter

[1] For some more background on surface layer meteorology and turbulence, see Appendix C

to a receiver through the ASL along a path of ∼100 up to 10,000m (Ward, 2017). The fluctuations in intensity measured at the receiver can subsequently be related to vertical fluxes of H and/or LvE dependent on the wavelength used (see Figure 1). Even though the method is less direct than the EC method, the spatially integrated nature of its output results in a larger and more constant footprint. Additionally, averaging in space instead of time allows for measurements at relatively high temporal resolutions. Consequentially, scintillometry has been regarded as a valuable addition to the field.

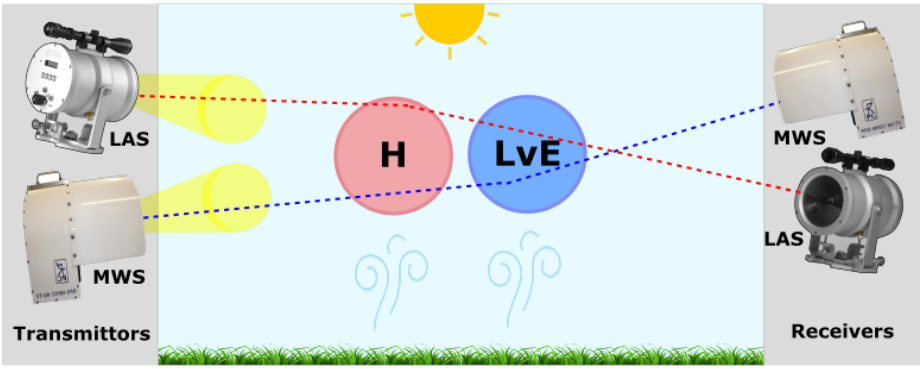

Figure 1: Visualization of a LAS-MWS scintillometer setup that is measuring turbulent fluxes in the ASL.

The current state-of-the-art method is biochromatic scintillometry, in which data from two scintillometers with complementary wavelength's (λ) are combined[2]. Also, large apertures of the optical (LAS) as microwave (MWS) antennas have also allowed for large separation distances ($\sim 5km$) between the transmitters and receivers. Recent studies have found this type of scintillometry a useful tool, with correlations coefficients (R^2) between the scintillometry and (aggregated) EC fluxes reaching values of 0.8-0.90 (Brunsell et al., 2011; Evans et al., 2012; Liu et al., 2011; Meijninger et al., 2006; Ward, Evans, and Grimmond, 2015). However, there are some key limitations to the method. For one, events with $+H$ and $+LvE$ cannot be distinguished from events with $-H$ and $-LvE$ due to sign ambiguity in the method (Ward, Evans, Grimmond, and Bradford, 2015). Furthermore, the Monin Obukhov Similarity Theory (MOST) - which is key in converting measured scintillations to fluxes (see section 2.2) - is known to vary between measurement sites and environmental conditions, especially for LvE (Kooijmans and Hartogensis, 2016). Other problems arise due to the large separation distances used in recent studies which are generally associated with heterogeneous land cover (well portrayed in Ward, 2017, Figure 3). Such heterogeneity violates MOST and results in well documented problems with validation due to footprint differences. In addition, the further the transmitters and receivers are apart, the higher they need to be mounted.

[2]For more information on key historical developments, see Appendix C

At $5km$ distance, this height is approximately 50m. Here, entrainment of dry air from the top of the CBL becomes significant, making it unclear whether the measured LvE is actually the surface flux(Braam et al., 2012). Furthermore, in stable atmospheric conditions it can occur that the surface layer is not $50m$ tall which disconnects the measurements from the actual surface conditions and again violates the assumptions behind MOST (Braam et al., 2012). As many of these issues are intertwined, there is a lack in understanding of the impact of each individual problem and how well state-of-the-art LAS-MWS scintillometry can be expected to perform under optimal conditions.

Herefore, we set up an experiment at the CESAR cite (NL), which is located in a well-watered near homogeneous meadow (Ruisdael Observatory, 2020). A LAS-MWS scintillometer was installed with a relatively short scintillometry path of $850m$. Consequently, the devices could be installed at a reduced height of $10.1m$ which limited entrainment and ensured the footprint represented the same surface as the validation methods. For validation, we used an EC-system, energy balance measurements, and a lysimeter, which were all located near the centre of the scintillometers' path. In parallel, we simulated the CESAR cite in a large eddy simulation (LES) to retrieve surface fluxes and perform 'virtual' scintillometer measurements (Kanda et al., 2004; Maronga et al., 2014). As far as we know, such parallel measurements have not been studied before. In this document, we show how we applied filtering and dynamic spectral cleaning to the RAW data, we explain how we navigated sign ambiguity with a newly developed dew detecting method, and we explore the impacts of MOST non-universality and entrainment on our measurements. We do this by answering the following research questions:

Main question:

- How reliable are the vertical fluxes of H and LvE as determined by state of the art LAS-MWS scintillometry under (near) optimal conditions?

Sub questions:

1. How can sign ambiguity associated with LAS-MWS scintillometry measurements be navigated?

2. Is Monin Obukhov Similarity Theory administered with universal MOST-coefficients valid for LAS-MWS scintillometry measurements at Cabauw?

3. To what extent are the vertical fluxes of H and LvE as measured with LAS-MWS scintillometry comparable to those measured with EC, and which method of processing the scintillometry data performs best?

4. To what extent do the structure parameters of temperature (C_T^2) and humidity (C_q^2) as measured by LAS-MWS scintillometry agree to those measured with EC?

5. To what extent are the virtual scintillometer patterns in the structure parameters (C_T^2 and C_q^2) and vertical fluxes (H and LvE) as observed in the LES representative of those in its footprint?

6. To what extent do the virtual scintillometer's structure parameters (C_T^2 and C_q^2) and vertical fluxes (H and LvE) compare to real life (best performing) LAS-MWS scintillometry measurements?

2 Theoretical Background

In this section we detail the theoretical background of the techniques we applied in our research. First, we explain the concept of structure parameters including an explanation of Kolmogorov spectra. Afterward, we provide an overview of scintillometry theory. If you are looking for more information about the methods used for Eddy Covariance or Large Eddy Simulations, see section 3.2 and 3.4 respectively.

2.1 Structure parameters

The spatial variability of any scalar can be expressed as a structure parameter C_X^2 . This variable plays a central role in scintillometry theory because it is a measure for the amount of turbulence in the atmosphere. Consequently, it will be one of the key variables in our analysis. While structure parameters can be retrieved in several ways, using the structure function displayed in equation 1 is most elemental (Beyrich et al., 2005):

$$C_X^2 = \overline{(X_{r_1} - X_{r_2})^2} r^{-\frac{2}{3}} \tag{1}$$

Here, X is the scalar of interest, r $[m]$ is the physical distance between points $r1$ and $r2$, and the horizontal line represent an average over a time interval. As the difference in magnitude of the scalar is squared, the sign of C_X^2 is always positive with larger values indicating more turbulence. In contrast, the sign of the cross-structure parameter C_{XY} can both be positive and negative. This variable indicates how one scalar covaries in space with respect to another. Its definition closely resembles that of the normal structure parameter and is shown in equation 2.

$$C_X^2 = \overline{(X_{r_1} - X_{r_2})(Y_{r_1} - Y_{r_2})} r^{-\frac{2}{3}} \tag{2}$$

Note that when applied to turbulence, the equations above are only valid within the inertial sub-range of the Kolmogorov spectrum (Kolmogorov, 1941). This theoretical turbulent spectrum describes atmospheric turbulence across all its various scales. It states that largest scales are the scales at which turbulent eddies are generated through for example heating and humidification of air at the earths surface.[3]. As these large eddies are forced through the boundary layer by buoyancy, they interact with other eddies which breaks them up into increasingly small eddies. The cascade down into smaller eddy scales is known as the inertial sub-range mentioned above. (Kolmogorov, 1941). When the eddies get smaller then the inner scale of turbulence, their momentum gets dissipated as heat through viscosity. Combined, these simple processes give rise to chaotic turbulence with eddies ranging from mm to km scales (George, 2010). The Kolmogorov spectrum also has practical applications, for example as an alternative way of calculating structure parameters. To do this, a time series (e.g. a 10 min interval) of the scalar should be converted to a spectral representation with the help of a fast Fourier transform (FFT) or equivalent method. From these spectra the structure parameter can be derived according to the following equation (from Hartogensis, 2006)

$$C_X^2 = 4k^{-\frac{5}{3}} S_X(k) \tag{3}$$

Here, S_X $[variancem]$ is the power at a specific k, and k $[\frac{1}{m}]$ is the radial wavenumber corresponding to this location. Importantly, this equation is only valid for k values within the inertial sub-range in the power spectrum. This inertial sub-range can be recognized by having a -5/3 slope in a semi-log plot (see figure 2). Averaging the resulting structure parameters over all k values within the inertial subrange results in a robust C_X^2 [4].

[3] Another common source of large eddies is located at the top of the convective boundary layer where entrainment of dry air from the free troposphere occurs

[4] A more thorough way of deriving C_X^2's from spectra is systematically layed out by Harto-

An important benefit of using a wavenumber instead of a frequency spectrum for meteorological data is that the location of the inertial sub-range becomes independent of wind speed. So, once this range is known it can be applied to other intervals of data. Additionally, this range can be used for calculating C_{XY} from a co-spectrum of two scalars, as it can be hard to identify an inertial sub range in such a spectrum. Besides that, the calculation of C_{XY} from a co-spectrum follows also follows equation 3. In the following section, which introduces scintillometry theory, structure parameters of several scalars act as intermediates to ultimately calculate surface fluxes with.

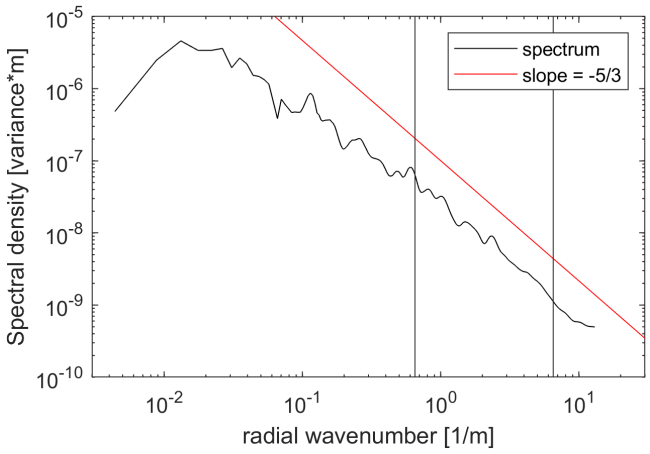

Figure 2: Example of a humidity (q) spectrum from 10 minutes of data at $10Hz$, with a distinctive $-\frac{5}{3}$ slope in its inertial sub-range. The vertical lines indicate the k region for which C_{Tq} was calculated and averaged into one value.

2.2 Scintillometry theory

This section describes common scintillometry theory, and will follow the steps detailed in table 1. In essence, the mathematical transformations explained in these steps reverse the cascade of events which caused the scintillations, to come back to the fluxes which generated the turbulent eddies. Note that reason that multiple intermediate variables are needed is a consequence of the indirect nature of the method.

Table 1: Detailing the steps associated with general scintillometer theory.

Step	Description	Associated variables
1	The scintillations measured by a scintillometer	$\sigma^2_{ln(I)}$
2	To structure parameters of the refractive index	C_n^2
3	To structure parameters of T and q and Tq	C_T^2, C_q^2, C_{Tq}
4	To the turbulent Fluxes through MOST	H, LvE, u_{star}, L_{ob}

gensis (2006) on his page 45. He systematically retrieves an averaged value for C_X^2 based only on those frequencies which are a part of the inertial subrange according to a strict quality control.

2.2.1 The scintillation index, $\sigma^2_{ln(I)}$

A Scintillometer can detect turbulent eddies by their influence on the signal, but the physical process behind this is not intuitive. first off, one should imagine a Scintillometers beam like a torch and thus not like a laser perfectly aligned with the receiver. Consequently, the scintillometer is not sensitive to refraction by large scale eddies as a small change in the angle of the entire beam will not cause the receiver to be out of the 'spotlight'. On the other hand, eddies much smaller than the aperture of the scintillometer won't influence the received intensity as most electromagnetic radiation can still directly hit the receiver. So, scintillometers are sensitive to eddies of approximately the size of the aperture (slightly larger for MWS). Additionally, one could imagine that individual eddies - with their associated temperature gradients and thus refractive power - act like lenses. They could converge or diverge the beam and thus the received intensity. While This effect does occur, it is only relevant for eddy sizes around the inner scale of turbulence (l_0), where dissipation starts (Tatarskii, 1971).

The received scintillations in LAS-MWS scintillometry are instead caused by the extinctions and amplifications of the signal's amplitude caused by diffraction of the transmitted electromagnetic radiation. Since this occurs when the beam unsyncs due to varying travelling time, it can be related to the refractive angle shift caused by turbulent eddies. For this reason scintillometers are most sensitive to turbulence in the centre of their path (as the smallest angels are needed here to cause extinctions). It is good to realize that the different wavelengths used in biochromatic-scintillometry require different angles to cause extinctions. In practice this means that they are sensitive to eddies of different sizes. This is solved by differing aperture sizes of the LAS and MWS which make both of them exclusively sensitive to parts of the inertial subrange of turbulence. As their sensitivity range known, the remainder of the turbulent energy spectrum can be projected. This forms the basis of the analytical relation between scintillations and the refractive index given in the next paragraph.

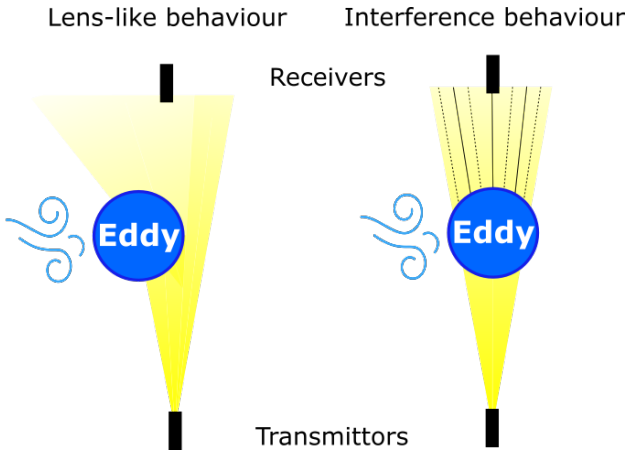

Figure 3: Conceptual figure of the effect of turbulent eddies on the scintillation signal. The example on the right *is* what phisically occurs. The effect on the left *does not* occur.

2.2.2 $\sigma^2_{ln(I)}$ to the structure parameter of the refractive index, C_n^2

Now that we have a feel for the way in which turbulent fluxes cause scintillations, we can start with the mathematical transformations associated with scintillometry theory. With the first 'causal step back', we find the structure parameter of the refractive index (C_n^2) caused by the eddies. This has been related to the variance (σ_x^2) and covariance ($\sigma_{x,y}$) of the natural logarithm of an intensity signal by Wang et al., 1978. The main equation suggested by them contains elements of wave propagation and turbulence theory which are combined and integrated over the scintillometers' path length (Wang et al., 1978). Equations 4 through 6 displayed below are the device-specific equations derived from the main one, which differ slightly with respect to eachother.

$$\sigma^2_{ln(I),LAS} = c_1 D^{-\frac{7}{3}} L^3 C^2_{n,LAS} \tag{4}$$

$$\sigma^2_{ln(I),MWS} = c_2 F^{-\frac{7}{3}} L^3 C^2_{n,MWS} \tag{5}$$

$$\sigma_{ln(I),LAS-MWS} = c_3 Max(F,D)^{-\frac{7}{3}} L^3 C^2_{n,MWS-LAS} \tag{6}$$

Here, c_1-c_3 are constants[5] [-], D is the aperture diameter [m], F is the Fresnel length ($\sqrt{\lambda L}$) [m], and L is the scintillometers path length [m]. Since all of these are known, the structure parameters (C_n^2) can be solved for.

2.2.3 C_n^2 to the structure parameters C_T^2, C_q^2 and C_Tq

The derivation of the structure parameters of T, q and Tq from the refractive index structure parameters is the next step in the processing chain (see table 1). Since the refractive index of air is dependent on T and q, it follows that the variability of the refractive index in space (e.i., C_n^2) can be related to the variability in T and q. Furthermore, the temperature sensitive nature of the λ_{LAS} and the humidity sensitive nature of λ_{MWS} should allow for a split between C_T^2 and C_q^2 to be obtained. This was proven to be possible by a theoretically derived from Hill et al. (1980) displayed in Equation 7 below.

$$C_n^2 = \frac{A_T^2}{T^2} C_T^2 + 2\frac{A_T A_q}{Tq} C_{Tq} + \frac{A_q^2}{q^2} C_q^2 \tag{7}$$

Here, C_T^2 is the structure parameter of temperature, C_q^2 is the structure parameter of humidity, C_Tq is the cross structure parameter of temperature and humidity, T [K] is the average temperature over the interval, q [$\frac{kg}{kg}$] is the average absolute humidity over the interval, and A_T and A_q [-] are wavelength dependent coefficients (see Ward et al., 2013 for a detailed description). As a separate version of Equation 7 can be made for each wavelength, two can be defined for LAS-MWS scintillometry. This is problematic since there are three unknowns

[5] Constants c_2 and c_3 are not entirely constant, but have a slight dependence on the measurement setup.

on the right-hand side (C_T^2, C_q^2 AND C_Tq), resulting in a closure problem.

Approaches of Hill and Lüdi

Two unique approaches emerged to tackle the closure problem. First, there is the 'Hill' or 'two-wavelength' method as proposed by Hill (1997). The method only uses the *variance* of the intensity fluctuations (thus equations 4 and5, also see Figure 4) and its solution falls back to basic turbulent eddy theory. It uses this to assume a value for the T-q correlation coefficient (r_{Tq}) which theoretically equals |1|. The positive 1 describes a situation at e.g. midday, where the energy input causes rising eddies to have both a higher T AND a higher q then their descending counterparts (and thus be correlated perfectly). A negative correlation coefficient can occur when descending eddies supply heat (-H) for evapotranspiration (+LvE), which commonly happens at night. Importantly, equation 8 can now act as a third equation which solves the closure problem. Problematically, the sign of r_{Tq} is ambiguous and the assumption of r_{Tq}=|1| is often violated, most notably during stability transitions. Therefore, it is common to use r_{Tq} values of ∼+0.8 ∼-0.6 which tend to be observed during experiments (see Ward, 2017 Table 1).

$$r_{Tq} = \frac{C_{Tq}}{\sqrt{C_T^2 C_q^2}} \tag{8}$$

In contrast, Lüdi et al. (2005) solved the closure problem by calculating an additional *covariance* term between the two scintillometers' intensity time-series (also see Figure 4). By inserting this variable into equation 6, C_{Tq} is obtained. As this allows for three variants of equation 7 to be calculated, the closure problem is also solved. Equation 8 can now be used to solve for r_{Tq} dynamically. Clearly, the covariance between the scintillometers' signals does contain valuable additional information. However, its noisy nature makes the resulting r_{Tq} somewhat unstable. Furthermore, nocturnal conditions with a positive r_{Tq} still lead to ambiguity as it is unclear if dew-fall is occurring or if the surface is losing stored energy. In the following section it will become clear how r_{Tq} defines the sign of surface fluxes.

2.2.4 C_T^2 and C_q^2 to the fluxes of sensible and latent heat

Monin Obukhov Similarity Theory is a frequently used framework by which to describe processes in the atmospheric surface layer (ASL) (Monin and Obukhov, 1954). In this framework, surface layer interactions are described by functions that scale with ζ, which is defined as $\frac{z}{L_{ob}}$. Here, z $[m]$ is the vertical height above the surface and L_{ob} $[m]$ is the Obukhov length. The Obukhov length can be interpreted as the height at which turbulence starts being predominantly

dependent on buoyancy instead of mechanical (wind driven) turbulence[6]. It is defined as follows:

$$L_{ob} = \frac{\rho c_p \theta_v u_*^3}{\kappa g H} \tag{9}$$

Here, ρ $[\frac{kg}{m^3}]$ is the density of air, c_p $[\frac{J}{kgK}]$ is the specific heat capacity of air (at constant pressure), θ_v $[K]$ is the virtual potential temperature, u_* $[\frac{m}{s}]$ is the friction velocity, κ [-] is the von kármán constant (=0.4), and g $[\frac{m}{s^2}]$ is the gravitational acceleration. While this framework has allowed for many insightful relations to be found, it is also quite restrictive due to its underlying assumptions of; stationarity (no advection of scalars), homogeneity (uniform and flat surface) and requiring measurements to be done within the surface layer (Monin and Obukhov, 1954).

Even though these requirements are hard to meet in scintillometry, the MOST relations between the structure parameters of T and q and the vertical fluxes of H and LvE are essential (see Figure 4). Problematically there is no analytical solution to be found for them, causing various empirical formulations to have been derived in the past (most notably by Andreas, 1988; Hill, 1992). While the empirically found equations should be identical according to theory (even at different measurement heights and over different surfaces), they tend to be substantially different. According to Braam, 2014 this uncertainty is caused by an array of factors such as; different environmental and meteorological conditions, varying instrumentation, MOST violations, and various data processing methods. Only recently Kooijmans and Hartogensis unified the MOST equations used in scintillometry by combining raw data from 11 different field campaigns which were gathered with identical equipment and processed with strict quality control[7]. As best portrayed in Ward, 2017 (their Figure 4), the new equations displayed below have a significantly reduced uncertainty and fall right in the centre of the other commonly used MOST equations.

$$f_{C_X^2}(\zeta) = \frac{C_X^2 z_{ef}^{2/3}}{X_*^2} \tag{10}$$

$$f_{C_X^2}(\zeta) = c_{X1}(1 - c_{X2}\zeta)^{-2/3} \qquad (\zeta < 0) \tag{11}$$

$$f_{C_X^2}(\zeta) = c_{X1}(1 + c_{X2}\zeta^{2/3}) \qquad (\zeta > 0) \tag{12}$$

$$H = -\rho c_p u_* T_* \tag{13}$$

$$LvE = -\rho L v u_* q_* \tag{14}$$

[6]For example; a value of +10 value would indicate predominantly mechanical turbulence at the surface, and therefore stable conditions.

[7]Ironically, the data gathered to empirically define these MOST relations is obtained using Eddy Covariance, since this is the most direct method.

Here, z_{ef} is the effective height (see Hartogensis et al., 2003), T_* and q_* are scaling variables of Temperature and Humidity, c_1 and c_2 [-] are the coefficients determined by Kooijmans and Hartogensis in 2016 (values in Table 2), and Lv $[\frac{J}{Kg}]$ is the latent heat of vaporization.

Table 2: Universal coefficients found by Kooijmans and Hartogensis (2016)

Unstable conditions ($\zeta < 0$)	$f_{C_T^2}$	$f_{C_q^2}$
c_1	5.6	4.5
c_2	6.5	7.3
Stable conditions ($\zeta > 0$)	$f_{C_T^2}$	$f_{C_q^2}$
c_1	5.5	4.5
c_2	1.1	1.1

Note that the sign of the fluxes is still undetermined after applying these equations. r_{Tq} is the variable which indicates the sign independent of the applied method. Generally, $r_{Tq} > 0$ means a positive H and a positive LvE (thus multiplying both the retrieved fluxes by -1) and $r_{Tq} < 0$ means a negative H and a positive LvE (Ward, Evans, and Grimmond, 2015). Furthermore, be aware that u_* is required to calculate the fluxes but cannot be retrieved from the LAS-MWS. Instead, it is common to use an additional anemometer and calculate u_* from its windspeed and an estimated roughness length. Equation 15 displays the relationship between these variables in which we used the Ψ-terms defined by Holtslag and De Bruin,1988.

$$u_* = \frac{kU_z}{ln(\frac{z}{z_0}) - \Psi_m(\frac{z}{L}) + \Psi_m(\frac{z_0}{L})} \tag{15}$$

Here, U_z $[\frac{m}{s}]$ is the windspeed at height z. It is important to mention that there is a strong interdependence between u_*, the L_{ob} and H in this last set of equations. Consequently, an iterative procedure needs to be used to calculate the fluxes. (Moene et al., 2004; Ward, Evans, and Grimmond, 2015). This wraps up the steps in figure 4 and therefore the established scintillometry theory. In the next subsection we will treat the main validation method in our research.

3 Methods

In this section we explain the methods we used in our analysis. Furthermore, we detail what choices we made while implementing the theory from the previous section. We will start with an overview of the research we did. Then we focus on scintillometry itself. Afterwards, we expand on Eddy Covariance, followed up by a section on entrainment tracers. Finally, we introduce our large eddy simulation (LES).

3.1 Research Overview

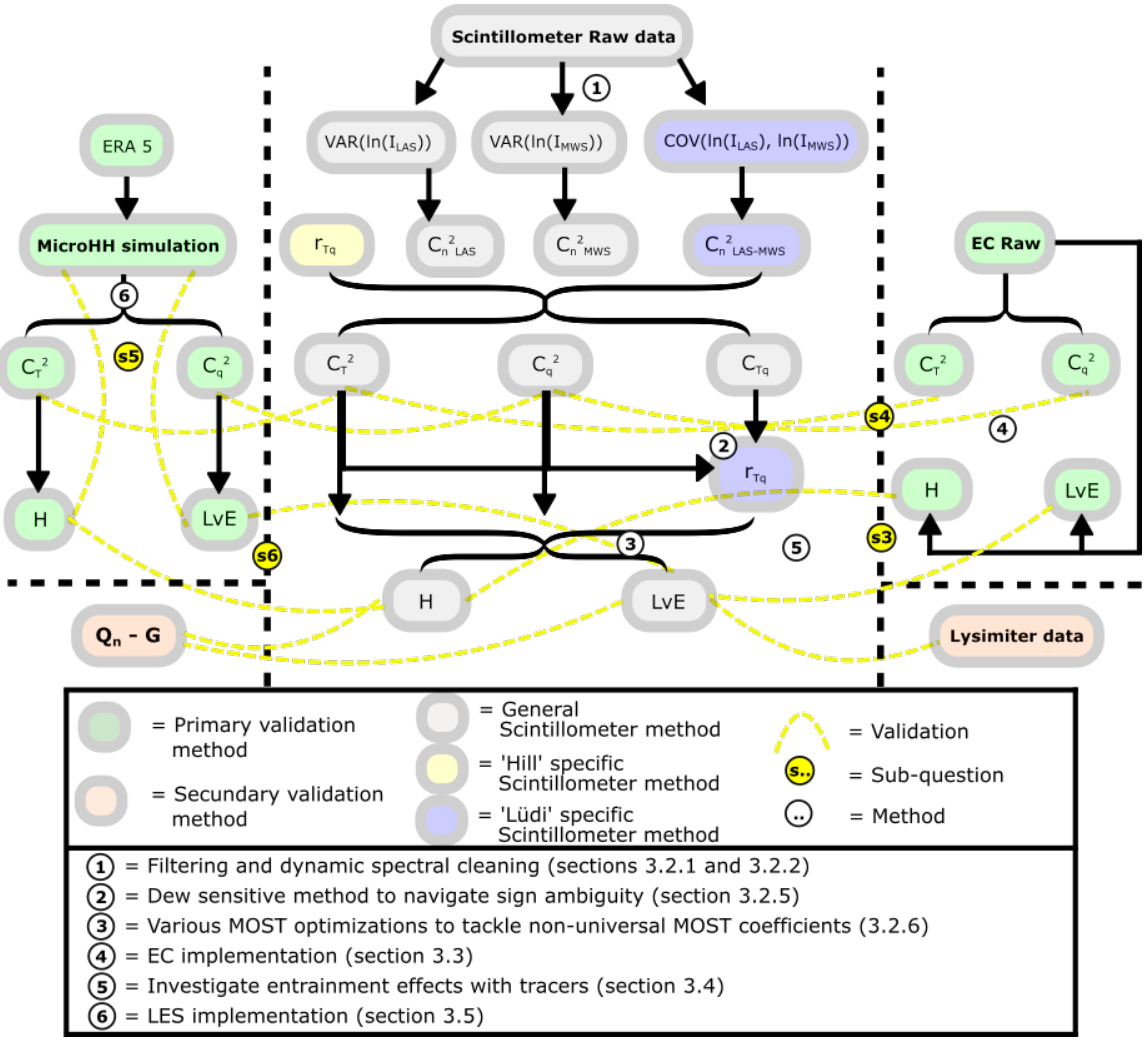

Figure 4: Overview of research described in this document.

3.2 scintillometry

Scintillometry has the advantage of making spatially averaged instead of local measurements. Due to this averaging, scintillometry can be used to calculate turbulent fluxes at relatively high temporal resolution compared to local techniques. We used intervals of 10 minutes of data to calculate our structure parameters and fluxes with, as this is the fastest temporal resolution with which EC method can reliably be used. This section first describes which steps were taken to filter and clean all LAS-MWS intervals, then we elaborate on our method to find the sign of the Hill approach, afterwards we explain the hybrid and dew detecting methods, and finally we detail our MOST optimization method.

3.2.1 $\sigma^2_{ln(I)}$ Filtering based on environmental conditions

We have filtered our data for rain and fog events. This is because obtrusions of the scintillation path causes a lower intensity to be measured at the receivers, without this being the result of turbulent eddies. In the surface layer, precipitation, fog, insects, and birds can cause such extinctions. While for the averaged flux measurements birds and insects don't cause serious errors, persistent rain and fog will. Herefore, any timestamp at which precipitation was recorded at CESAR was removed even though interestingly large values for LvE were expected [8]. Events like fog and condensation which reduced the received intensity of the LAS by more than 88% were removed. One could argue that nocturnal conditions should be filtered away too because buoyancy is suppressed which causes the exchange of heat and water vapour to be relatively small[9]. Consequently, the absolute error during night-time scintillometer measurements is often large compared to the fluxes. Still, we chose to calculate these fluxes while keeping in mind their limited reliability. The combination of these actions should limit the presence of erroneous fluxes caused by disturbing environmental conditions.

3.2.2 $\sigma^2_{ln(I)}$ Spectral cleaning

After accounting for disturbing environmental conditions the data was cleaned for tower vibrations, humidity adsorption fluctuations, changes in opacity and interference of electrical equipment (Meijninger et al., 2006). Problematically, such influences can occur continuously and are superimposed on the signal you do not want to lose, which makes removing entire intervals undesirable. The tool to eliminate such unwanted artifacts is spectral analysis. We converted the scintillation time-series of every interval into a spectral representation through a fast Fourier transformation (FFT) (or equivalent method). In layman's terms,

[8] While H and LvE fluxes are dodgy, measuring area averaged rainfall intensities with scintillometry is an interesting additional feature suggested by Upton et al., 2005.

[9] One exception to this are nights with strong winds, in which mechanical turbulence is stronger then the stratification caused by surface cooling. On the contrary, wind speeds tends to be lower at night and the surface layer resulting from mechanical turbulence is generally shallow.

this spectral representation indicates the strength of the frequencies out of which the time-series is built up (see Figure 5 for an example). Since the shape of the theoretical spectrum and its frequency shift dependent on the cross-wind speed (U_{cross} $[\frac{m}{s}]$) are known, the effect of other unwanted signals can be removed[10]. After spectral filtering is applied, the cleaned time-series can be retrieved by applying an inversed fast Fourier transform (IFFT).

In our data processing we have applied a high pass filter (HPF) and a low pass filter (LPF) to each spectrum in order to remove the influence of signals with unrealistically low and unrealistically high frequencies (Meijninger et al., 2006). The HPF and LPF we used were dependent on the cross-wind speeds measured during each interval (as suggested by Ward, 2017). Since the shape of theoretical spectrum can be calculated for a given U_{cross}, we were able to set the HPF and LPF such that a set percentage of the theoretical spectrum's variance was retained (after Stoffer, 2018). We chose a LPF which retained 99% of the theoretical variance, and a stricter HPF which only retained 95% since our data contained more noise at lower frequencies. Furthermore, we used the mean of the slowest 50% of windspeeds to determine the HPF and the other half for the LPF instead of using the global mean for both. This allowed us to take into account the variability of U_{cross} within an interval, which broadens the theoretical turbulent energy spectrum (see Figure 5). During strong winds blowing parallel to the scintillometers path some problems arose. Here, the Ucross component can be near zero while a shift in the location of the spectrum is still observed. To prevent an erroneous band pass filter (BPF) from being selected, we incorporated 20% of U into U_{cross} when $\frac{U}{U_{cross}} > 5$ which increased both averages progressively. Put together, this dynamic method ensured proper BPF selection.

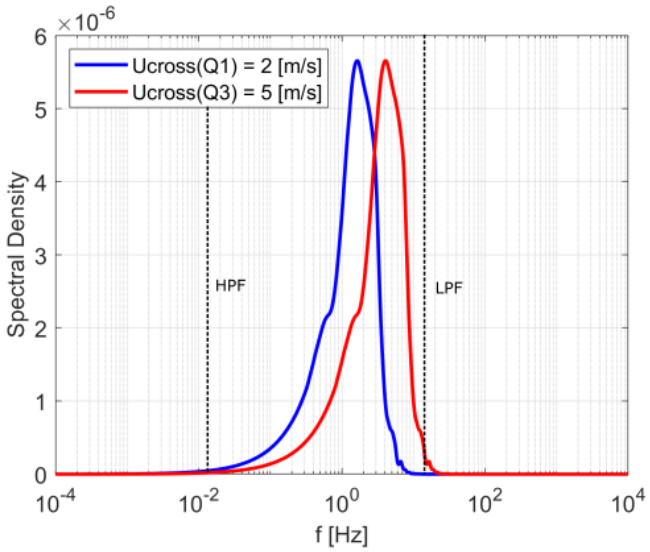

Figure 5: Theoretical spectrum of the scintillations measured with a scintillometer. Note that the location of the theoretical spectrum is dependent on the cross-wind speed

[10] See: Van Dinther et al., 2013 for an in-dept analysis of U_{cross} on turbulent energy spectra.

3.2.3 Innovation in C_n^2 processing: Flux sign using Hill

The main weakness of the Hill method is that r_{Tq} is not solved for. Consequently, the sign of the fluxes is ambiguous. To solve this, we designed an algorithm which is able to identify the daily transitions from stable to unstable and back. It is based on the time-series of H calculated under the assumptions of stability ($r_{Tq} = 0.8$) and instability ($r_{Tq} = -0.6$). As can be seen in the example in figure 6, the transitions from daytime instability into night-time stability are visible as a low in the unstable timeseries and a high in the stable timeseries. Furthermore, this example day shows two transitions like the theory suggests, one in the morning and one in the afternoon. So, after the morning transition unstable conditions with a positive r_{Tq} occur during daytime, returning to stable conditions with a negative r_{Tq} after the afternoon transition. Finding the correct moments for transition for each day in our dataset was the goal of this algorithm. It works by finding the transition points at which the lowest 5 values in the unstable time-series occur closest in time to the highest 5 stable values (see figure 6). If several lows and highs are 'as synced in time', the average timestamp will be selected as the transition point. While this approach may seem overly complicated, it is more rugged then simpler methods on days which have poorly defined stability transitions.

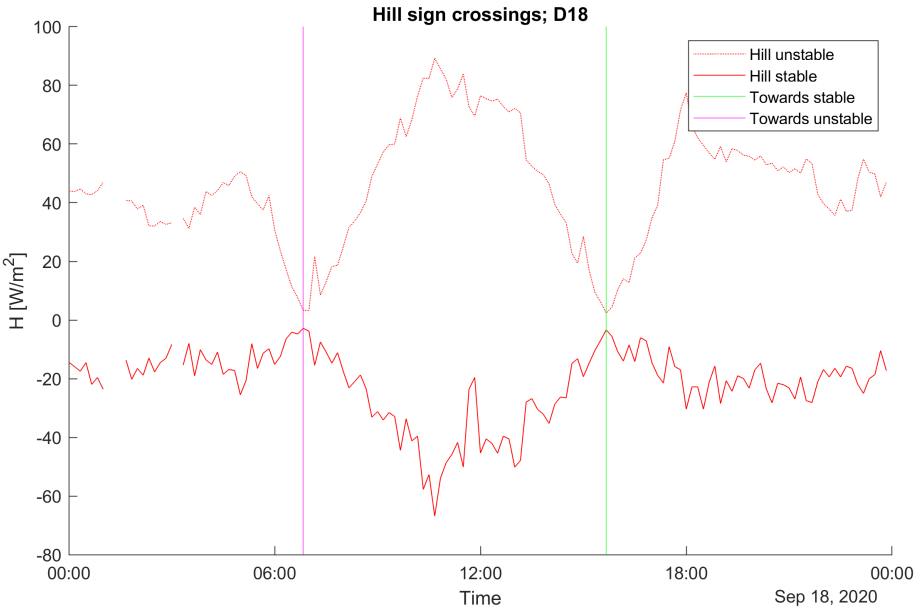

Figure 6: Example of stability transitions determined by our algorithm

To further increase the algorithms rigidity we made it sensitive to the transition points of surrounding days. This information should be meaning full as the stability transitions at one location under similar environmental conditions are

not expected to deviate much. After calculating the transition points for all separate days, we aggregate them to calculate a nominal transition time. We defined this nominal transition time as the 60^{th} quantile of the various morning transitions and the 50^{th} quantile (median) of the various afternoon transitions. This has advantages over the mean as it excludes outliers and compensates for the increased likelyhood of erroneous transition points in the early morning, where fluxes are small and errors large. Finally, by looking for minima and maxima within a $\tilde{3}$ hour window around the nominal transition instead of looking at half a day, highly dynamic yet reasonable transition points were found.

3.2.4 Innovation in C_n^2 processing: Hybrid method

To use the benefits of both the Hill and L udi methods a third 'Hybrid' method has been proposed by Stoffer (2018). As this method is promising but hasn't had a lot of validation, we included it in our analysis. He defined criteria by which unrealistic values for r_{Tq} as resulting from the Lüdi method are replaced by their 'Hill' counterparts. The replacement values are r_{Tq}= 0.8 OR -0.6 dependent on the sign of Lüdi's r_{Tq}, instead of unrealistic assumption of r_{Tq}=|1|. Subsequently, erratic sign changes in r_{Tq} - defined as a value preceded and followed up by values with the other sign - are replaced by the average r_{Tq} of its neighbours. Finally, Stoffer applied a moving average (window=5) to the time-series of r_{Tq} to increase its stability. The combinations of these rules should creates a method with a more realistic output fluxes. However, like the Hill and L udi methods, the hybrid method is unable to separate dew events with $-H$ and $-LvE$ from unstable events with $+H$ and $+LvE$.

3.2.5 Innovation in C_n^2 processing: Dew detecting method

One fundamental problem with current scintillometry theory is the lack of a way to determine the sign of the fluxes without using external tools. Both the Lüdi (thus Hybrid) and the Hill method (including our a transition algorithm) only solve this problem partially. We found out that a combination of both approaches should theoretically solve the sign problem in its entirety. It works as follows: A day can be divided into a generally stable night-time section and a generally unstable daytime section. When r_{Tq} is positive during the daytime section, it follows that both H and LvE are positive. Alternatively, during the night-time section a positive r_{Tq} is likely to indicate dew-fall [11]. Importantly, a negative r_{Tq} is not ambiguous and indicates a negative H and a positive LvE. As there generally are well defined morning and afternoon dips in r_{Tq}, we can smoothly transition between both 'modes' of $r_{Tq} > 0$ (see table 3). An example of these dips can be found in figure 7.

[11] This claim is true for the natural environment. For urban environments, positive H and LvE can occur during nighttime as (stored) heat is released from buildings and roads (see section 6.4)

Table 3: Conceptual table describing the transitions within the dew detecting method.

	Regime	
	night	day
$r_{Tq} > 0$	$-H$, $-LvE$	$+H$, $+LvE$
$r_{Tq} < 0$	$-H$, $+LvE$	$-H$, $+LvE$

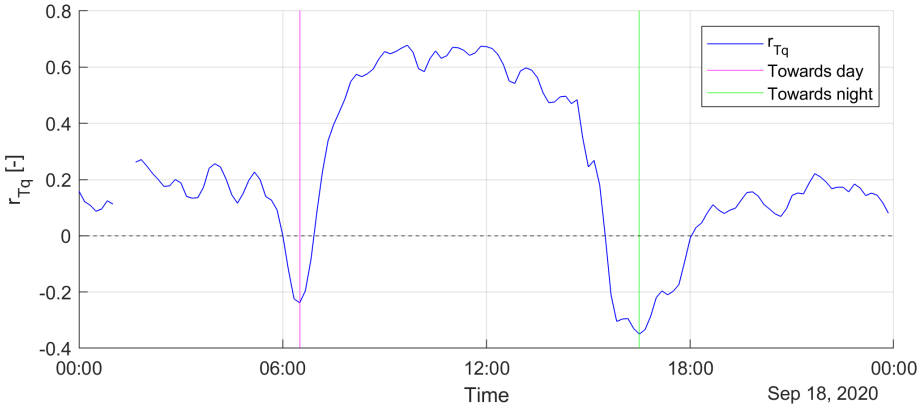

Figure 7: Example of stability transitions determined by sign swap algorithm

As was the case for our determination of the sign of the fluxes from hill, not all days have as well defined transition points. Consequently, we adopted a similar strategy of introducing information from the surrounding days to limit the region in which minima can be found. We did this by first finding all morning (00:00-12:00) and afternoon (12:00-24:00) minima for the individual days. Then we calculated the nominal morning and afternoon transition points for each day based on a moving average with a window of 11 days (i.e. the 5 previous and 5 consecutive days). Finally, each transition point is defined as the minimum in r_{Tq} within a three-hour window around that days nominal transition time. Put together these steps result in a highly dynamic method for solving the sign of the fluxes without any remaining ambiguity.

3.2.6 C_T^2 C_q^2 to fluxes: MOST optimization

Even though Monin-Obukhov similarity theory should be universal, its coefficients are known to be influenced by environmental and meteorological conditions, especially for determining LvE (Kooijmans and Hartogensis, 2016). Therefore, the coefficients found by Kooijmans and Hartogensis might not be optimal for our measurement site. Since our setup consists of a scintillometer and an EC-system with similar footprints, we were able to optimize the MOST

coefficients in a somewhat unconventional way. The essence is that the best MOST coefficients should result in scintillometer fluxes which are most similar to EC fluxes. We were able to test this by solving for a variant of the coefficient of determination (R^2) between the EC and Scintillometer time-series ((Equation 16). This variant compares y to the 1:1 line (thus x) instead of a regression line.

$$R^2_{1:1} = 1 - \frac{\Sigma(y-x)^2}{\Sigma(y-\overline{y})^2} \tag{16}$$

As the neutral limit (given by c_1) is known to be approximately 5, we made an algorithm run through all possible MOST combinations of $4 <= {c_1}^{12} <= 6$ and $c_2 >= 0$ to find the best set (Kooijmans and Hartogensis, 2016). Here, it is important to first optimize the temperature coefficients by finding the best fit for H (see table 2). This is because the best fit for LvE is determined by both temperature and humidity coefficients since the magnitude of H influences ζ. Furthermore, since the scintillometer and EC system assumed different signs for LvE during some intervals, we adjusted the scintillometers signs to equal those from EC during optimization. When we did not do this, the optimization tried to mitigate the effect of the erroneous signs by reducing the magnitude of the fluxes, and thus reducing the accuracy those intervals with the correct sign. Apart from these obstacles, the methods implementation is straightforward.

3.3 Eddy Covariance

In this subsection we briefly explain the Eddy Covariance technique for measuring fluxes and structure parameters. After this we will detail how we filtered the EC data. We calculated the fluxes and structure parameters over 10-minute intervals like we did for scintillometry. This interval duration is on the short side of what is physically possible with EC.

3.3.1 Fluxes

EC is a direct method specifically designed for determining the fluxes of H and LvE. It does this by measuring the vertical movement (w), T, and q of the eddies themselves. The transformations required can be expressed in one equation for either of the vertical fluxes:

$$H = c_p \rho \overline{w'T'} \tag{17}$$

$$LvE = Lv\rho \overline{w'q'} \tag{18}$$

[12] When the coefficients of 2016 (2016) indicated a value of 5.5, we allowed for values up to 6.5, thus allowing for a difference of |1|.

Here, w $[\frac{m}{s}]$ is the vertical wind speed, $'$ denotes the fluctuation component after Reynolds decomposition, and the horizontal line represents a time average. Under ideal circumstances the resulting fluxes would be realistic but in practice several corrections are applied to prevent artifacts from distorting the measurements (see e.g., van de Boer (2015)). Detrending is one of these and is meant to prevent the influence a gradual change in the magnitude of a scalar during the measurement interval. If this correction is not applied a sharp temperature rise would make it seem like T' was negative for the first half of the interval and positive the second half, thus losing all co-variation with w'. Furthermore, a T_{sonic} correction is important as it counteracts the influence of humidity in the temperature signal. Finally, rotations ensure that $\overline{w} \equiv 0$ by adjusting the pitch and jaw of the EC's coordinate system. This prevents the advection U - which is generally much larger then w - to nullify the w' signal when the EC is not perfectly aligned to the wind. Additionally, the EC was rotated in such a way that all advection is contained in $\overline{u}$, causing $\overline{v} \equiv 0$. While more corrections are often applied to EC data, we only applied these three to every interval of EC data as they are most essential.

3.3.2 Structure parameters

EC corrections are also important for determining structure parameters from EC measurements. The general equations for calculating these require simultaneous spatially separated measurements, and therefore don't apply to single point measurements like taken by an EC-system. If only one EC-station is present, the 'Taylor hypothesis of frozen turbulence' can be applied. It assumes that when turbulent eddies get horizontally advected by wind, their physical structure remains unchanged. This allows for the spatial separation ($r1$ to $r2$) to be replaced by a temporal separation ($t1$ to $t2$) dependent on U.

$$C_X^2 = \overline{(X_{t_1} - X_{t_2})^2}(\Delta t U)^{-\frac{2}{3}} \tag{19}$$

Like is the case for the general equation, C_{XY} can be calculated by multiplying δX by δY instead of squaring δX. Note that the spectral method of determining structure parameters can also be applied to EC measurements.

3.3.3 Data filtering and cleaning

The main uncertainty in the EC data comes from the infra-red gas analyser (IRGA). It is used to determine the absolute humidity of the air (Q) and can give erroneous outputs during and after rain events or when its path is obstructed in another way. The data was filtered for $0 < Q < 1200$ $[\frac{mmol}{m^3}]$ (~ 0.02 $[\frac{kg}{m^3}]$). Furthermore, C_T^2 resulting from EC was filtered for $0 < C_T^2 < 0.4$ $[K^2 z^{-2/3}]$, C_q^2 for $0 < C_q^2 < 4e^{-7}$ $[\frac{kg}{kg}^2 z^{-2/3}]$ and C_{Tq} for $-10^{-4} < C_{Tq} < 10^{-4}$ $[K\frac{kg}{kg} z^{-2/3}]$ to keep them within reasonable limits. For the same reason H was filtered for $-80 < H < 300$ $[\frac{W}{m^2}]$ and LvE for $-40 < H < 350$ $[\frac{W}{m^2}]$. We deem such crude

data filtering justifiable as EC is our validation method which should be stable and realistic.

3.4 Tracers for non-local influences

The scintillometry and EC methods are aimed at calculating the surface fluxes. In practice, entrainment fluxes at the top of the boundary layer - most notably the introduction of dry air into the boundary layer - influence the measurements. In this subsection we describe two tools which we used to identify such non-local effects.

3.4.1 Skewness

The skewness of ground-mounted high frequency humidity signals has been used as tracer for entrainment effects (Esters et al., 2020; van de Boer, 2015). It works as follows: When no entrainment occurs within an interval, there is no significant gradient in q at the top of the CBL. This causes all descending eddies to have similar values for q. A histogram of q would herefore skew to the right (positive), as no outliers are present for low values of q (see figure 8). In contrast, there would be hardly any (or even negative) skewness during entrainment events as the gradient in q causes (very) dry parcels of air to reach the surface too (van de Boer, 2015).

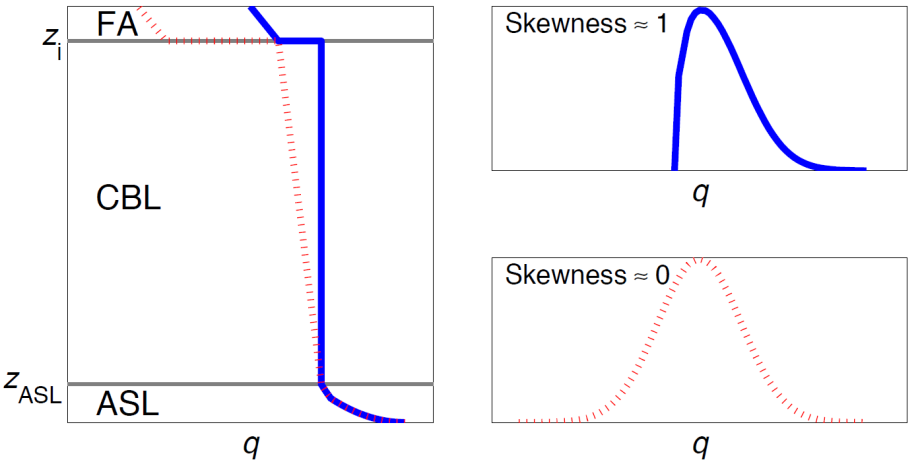

Figure 8: Explanation of the effect of entrainment at the top of the atmosphere on the skewness in q. This figure was taken from van de Boer, 2015.

The skewness (S) value can be calculated from a time-series with equation 20 below.

$$S_q = \frac{(q - \mu_q)^3}{\sigma_q^3} \tag{20}$$

Here, μ_q is the average value of q and σ_q is the standard deviation of q. It turns out that the skewness in q during daytime ranges from approximately zero to one above land when it is scaled with σ_q^3. An advantage is that this tool is not exclusive to EC as no high frequency anemometer is needed. A weakness of the skewness is its sensitivity to both vertical and horizontal non-local influences (Esters et al., 2020). Therefore, a complementary method as described in the following section is welcome.

3.4.2 Quadrant analysis

A quadrant analysis is an extension of the normal flux calculations with EC as described above. Instead of aggregating all positive and negative contributions of $\overline{w'X'}$, they are segregated into four separate fluxes like is shown in figure 9 below. Importantly, the sum of the fluxes calculated from the four components should equal the total flux. While quadrant analyses are used for segregating various types of fluxes, our focus is on entrainment which has the strongest effect on LvE. The ratio of the 3rd quadrant of the LvE flux compared to the total flux is expected to be larger during entrainment effects and smaller when no entrainment occurs. This ratio will therefore be the tool with which we identify entrainment events.

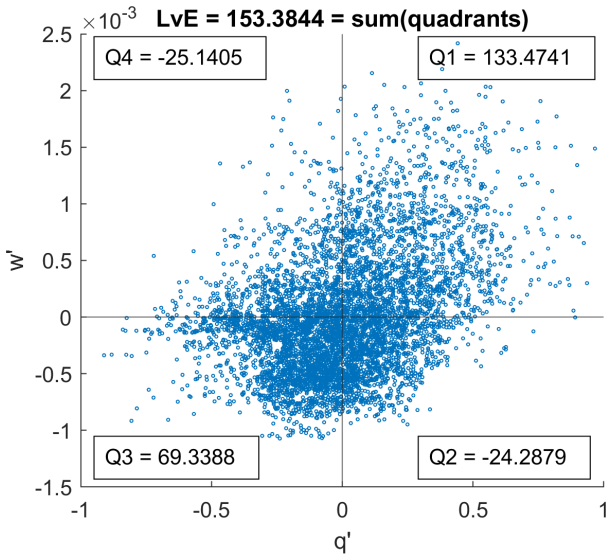

Figure 9: Example of a positive LvE segregated into quadrants. Based on 10 minutes of 10Hz EC data measured at 3 meters height at Cabauw (NL) on 14-09-2020 at 12:00.

3.5 Large Eddy Simulation

Large Eddy Simulations (LES) are being used to simulate flow - including turbulent flow - in high detail. They are grid based (2D or 3D) numerical models in

which the governing equations of fluid dynamics (i.e., Navier-Stokes) are baked in. Common applications for such models are the simulation of aerodynamics in e.g., aviation (e.g. Sagaut and Deck, 2009), optimization of combustion engines (e.g. Richard et al., 2007), and (partially) resolving turbulence in the convective boundary layer (CBL)(e.g. Pasquariello et al., 2017, Maronga et al., 2014). The limiting factor of all LESs is computational power. We used a relatively simple $768x768x288$ grid setup for simulating 9 hours of atmospheric turbulence. This run took 67 hours on a supercomputer with 1536 CPU cores (approximately 100.000 CPU hours). As our domain covered $5.3km^2$ the grid spacing doesn't come close to the mm scale involved in real turbulence. Consequently, other approximations are used to mimic the turbulent effects at smaller scales. Below we will first describe the model, its settings, and the inputs used for our LES. Then we will detail the outputs of our LES and how we manipulated these to calculate suface fluxes and make virtual scintillometer measurements.

3.5.1 microHH

We used a newly developed model for making LESs called microHH (μHH) (Van Heerwaarden et al., 2017). It uses various schemes to solve relevant interactions which are separate from the general Navier-Stokes equations between the grid cells. Table 4 summarises the essential schemes and refers to the origin these parameterizations. The land surface model in specific is highly detailed and simulates the behaviour of plants and their stomata in detail. Additionally, it contains four distinct soil layers with dynamic moisture contents which determines the drought and water stress of the vegetation. Note that the energy balance was forced to close in our LES, like would theoretically be expected. One key advantage of microHH is its ability to spread its workflow among multiple computing cores, including GPU's. This allows the model to be faster then conventional LES models, allowing for simulations with higher resolutions to be run.

Table 4: This table describes the relevant scemes used in the microHH model to run our LES. For further details, see Van Heerwaarden et al. (2017)

Sceme	Name	Reference
Sub-grid	Smagorinski	Smagorinsky, 1963
Advection	Wicker-Skamarock	Wicker and Skamarock, 2002
Radiation	RRTMGP	Pincus et al., 2019
Land surface	HTESSEL (simplified)	Balsamo et al., 2011
Surface layer	Monin-Obukhov	Van Heerwaarden et al., 2017

The LES used in our research simulates the Cabauw site (CESAR, NL) and its surroundings within a horizontal domain of $2300x2300m$. Each individual grid-box covers $3x3m$ and the centre of the domain is located at 51.96998°N and 4.93697°E. The land use classification for each of these boxes was based on the Top10NL dataset. Note that the domain was rotates clockwise by $\sim 6°$'s with

respect to true northing as an inheritance from a previous simulation. Along the vertical axis (z), the simulation reaches from 0 to $2800m$, where the first 600 meters have equidistant grid-boxes with a height of $3m$. The consecutive grid-boxes were made increasingly tall as they describe the less relevant free troposphere. The LES was initialized and forced with ERA5 data. Since the ERA5 grid is course compared to the LES, it takes some time and thus space (advection) before turbulence has developed. To counter this, the advection leaving the model re-enters the model at the other side of the domain. Also, the LES was spun up for more then $10km$ of advected distance to ensure well developed turbulence during the entire simulation period. The time interval which was simulated ran from 9:00 to 15:00 on the 14^{th} of September 2020. This day had the benefit of being relatively sunny and warm for the time of year. In the next sections we detail how we used the output from the LES.

3.5.2 Surface fluxes

Surface fluxes were derived from the LES data analogously to EC flux calculations (see equations 17+18). For this purpose, the $\overline{w'q'}$ and $\overline{w'T'}$ components were saved at a 30 second interval for the entire surface the LES domain. For ρ we used the domain averaged surface values instead. Subsequently, we averaged the calculated fluxes over a 10 minute interval, like we did for the real and virtual scintillometer measurements. Figure 10 shows a intermediate output of the surface fluxes.

The rotation to true northing of the LES domain shown in Figure 10 was applied because we have used a footprint model to determine the surface fluxes influencing the scintillometer and EC system respectively. This footprint model works like the one described by Meijninger et al. (2002). It uses the wind direction (WD), wind speed (U), measurement height (z), Obukhov length (L_{ob}) and standard deviation of the cross-wind speed (σ_v) to find where on the surface the eddies observed by the measurement device originated. Calculating the footprint of an EC station is relatively straightforward but, calculating one for a scintillometer is more complex as it makes spatially averaged measurements. Meijninger et al. (2002) solved this by making a footprint for every point on the scintillometers path and averaging these footprints with the scintillometers path weighting function. The output of such a footprint model is a two-dimensional map with weights associated to every grid cell in the domain (w_{xy}). As $\Sigma\ w_{xy} = 1$, it can be multiplied to a surface variable to find the averaged value within the footprint. In the LES we used the same location and height for the scintillometer and EC as where they were installed in real life to maximize comparability. Furthermore, this allowed for the footprints to be based on 10-minute intervals of real EC data and thus not on the LES output itself. Ultimately, the surface fluxes from the scintillometer and EC footprints were expressed as timeseries with the duration of the LES simulation and with an interval of 10 minutes.

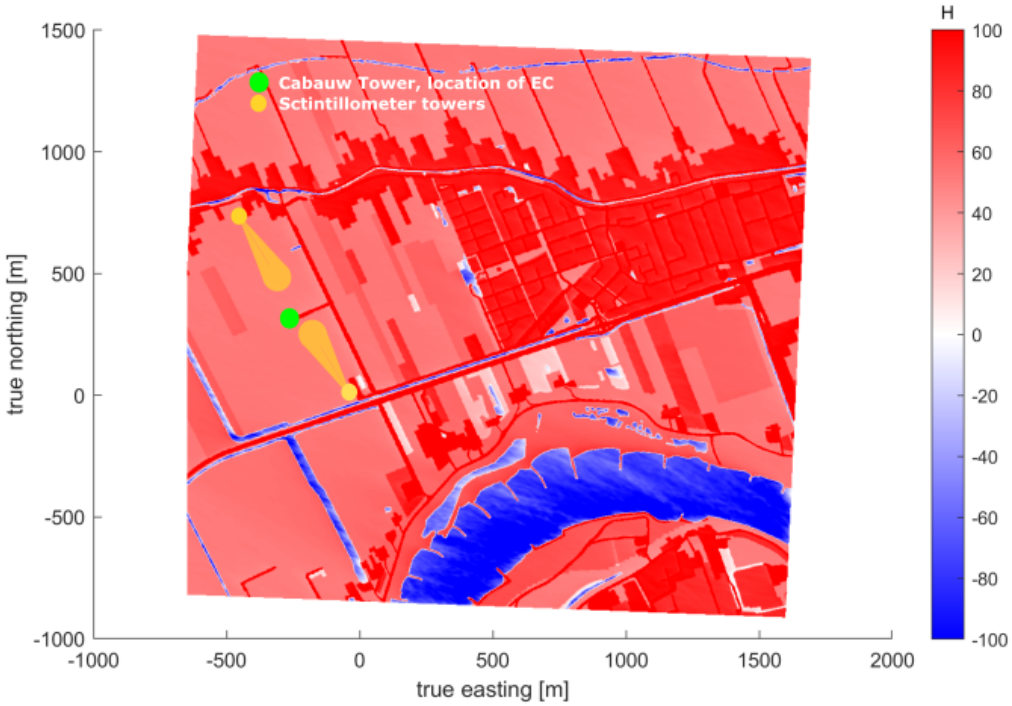

Figure 10: 10 minute average surface sensible heat flux over the LES domain around the CESAR site (NL). The field has been rotated to align with true north. 0,0 indicates the location of the scintillometer receiver

3.5.3 Virtual scintillometer measurements

As explained in the theoretical background section, real scintillometry measurements are based on the received intensity fluctuations. By using an advanced direct numerical simulation (DNS) it could be possible to make such measurements in a virtual environment. However, since we used a simpler and courser LES, we enter the scintillometer processing chain at the (co)structure parameters of T and q instead (see figure 4). To this end, we saved 1Hz T and q data along the entire scintillometer path consisting of 286 grid-boxes. Subsequently, we applied both the structure function definition (equation 1) and spectral technique (equation 3) described in the theoretical background to derive the structure parameters from these. The difficulty here is the two-dimensional nature of the data involved.

For the structure function method we first calculated the (co)structure parameters for a separation distance of $21m$ along the entire path with equation 1. Then, we averaged these point measurements over 10-minute intervals. Finally, we used a path weighting function to find a weighted average along the entire path. Figure 11 visualizes how this two-dimensional data is aggregated into one time series. The physical separation distance r with which to determine the initial (co)structure parameters was found empirically by testing which separation distance results in the largest structure parameter (figure 12). Too short separation distances underestimate these due to the limited resolution of the LES which washes away variations on scales smaller than the grid size. Contrarily, too large separation distances get larger than the largest eddy sizes, which averages out the influence of individual eddies[13].

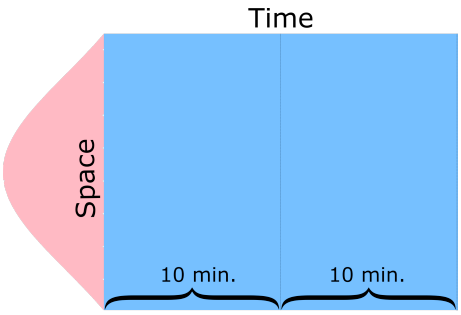

Figure 11: Conceptual picture indicating how we aggregated two-dimensional C_X^2 data derived from the structure function definition (equation 1) into one value for C_X^2 representing the virtual scintillometer measurement.

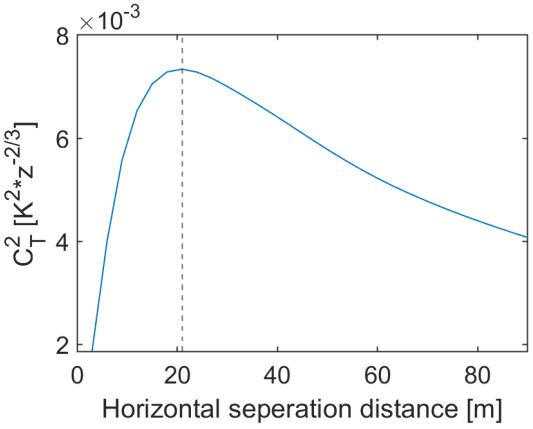

Figure 12: This figure compares the value of C_T^2 to the horizontal separation distance with which it was calculated (equation 1). The peak at $21m$ represents the inertial sub-range.

An alternative way in which we calculated the co(structure parameters) was by using Kolmogorov spectra (similar to Maronga et al., 2014). To do this, we calculated a frequency spectrum for every 10-minute interval on all locations along the path. Furthermore, we converted these to radial wavenumber spectra by using the U measured at each gridbox. As these spectra consist of only 600 measurements, they are ill-defined. By aggregating these spectra across space using a path weighting function, we found one representative that was much smoother (same logic as figure 11). These aggregated spectra can be seen in figure 13.

[13]Turbulent eddies can reach scales up to the kilometre scale. However, these are measurements from $10.5m$ above the surface which limits the size of the largest eddies

The fact that only a tight inertial sub-range is present in these spectra is in line with the lack of a plateau in figure 12. The structure parameters were subsequently calculated for the k's in the inertial subrange according to equation 3.

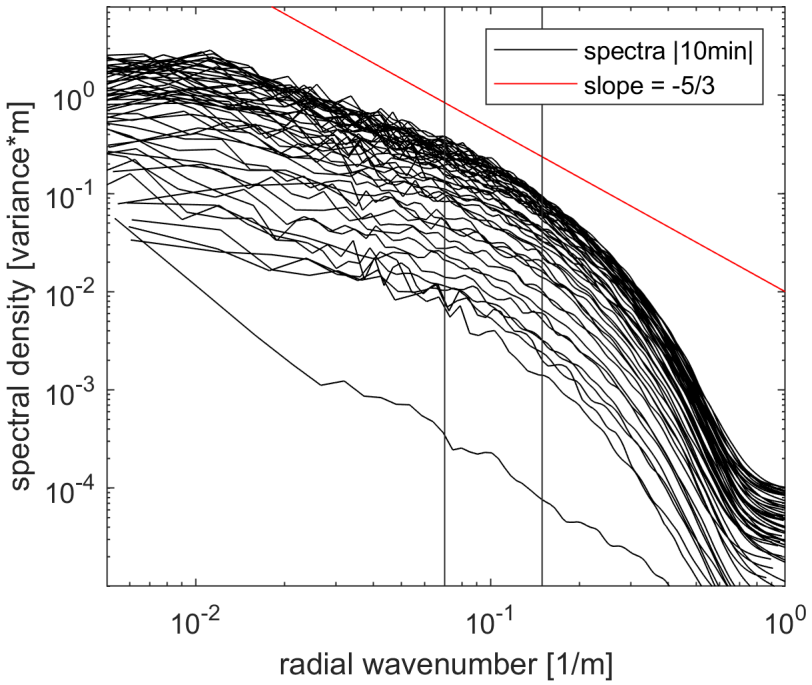

Figure 13: Here, every black line represents a set of T spectra (10 minutes), converted to radial wavenumbers and aggregated over space. The red line indicates the slope an inertial subrange should have. The vertical black lines define the range of k's for which C_T^2 was calculated according to equation 3.

After we derived C_T^2, C_q^2, and C_{Tq} from the two methods described above, we converted them to fluxes like we did for the real scintillometer (see section 2.2.5). Additional variables like ρ, θ_v, humidity corrected c_p, temperature corrected L_v and U were taken from the scintillometers path, and averaged into one value per interval using a path weighting function. z_0 was land-use dependent so we used the same footprints used to calculate weighted average surface fluxes to retrieve one representative z_0 per timestamp (figure 37, Appendix B).

4 Data description

The well watered, homogeneous meadow over which the LAS-MWS scintillometer was set up is located near the village of Lopik in the west of the Netherlands. This location is famous for its large meteorological tower of $213m$, often referred to as the Cabauw tower ($51.97027°N$, $4.92625°E$).

The Cabauw Experimental Site for Atmospheric Research (CESAR) of which this tower is a part is located at $0.7m$ below sea level and is has no more then a few metres of elevation change present for over $20km$ (Ruisdael Observatory, 2020).
The transmitters and receivers of the two scintillometers have been placed at $10.1m$ height on vibration free towers build for astronomical purposes. The transmitters' tower is located $480m$ NNW of the Cabauw tower ($51.97425°N$, $4.92348°E$) and the receivers' tower at $380m$ SE of the Cabauw Tower ($51.96753°N$, $4.92961°E$). This makes for a total beam length of $856m$ (see Figure 14). Since the south-westerly prevailing wind direction is (near) perpendicular to the scintillometer path, its general footprint is as large as possible and doesn't contain obstacles for about $2km$.

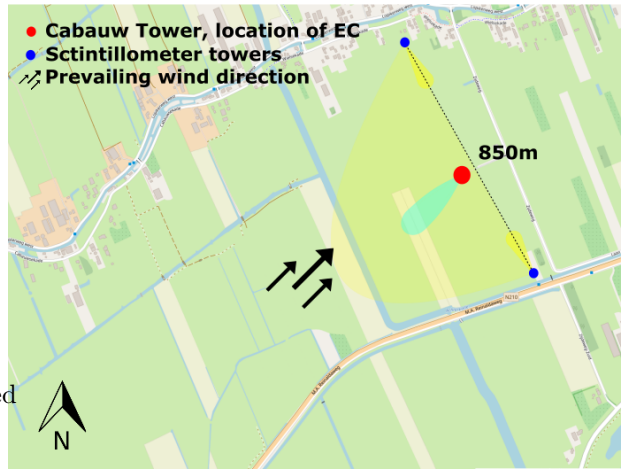

Figure 14: The CESAR measurement site located west of Lopik (NL). The yellow and turquoise shades resemble the scintillometers and EC footprints respectively.

The Large Aperture Scintillometer installed at CESAR is a Kipp & Zonen LAS MkII ($850nm$). Its received analogue scintillation signal was directly transferred to the microwave scintillometer receiver placed $35cm$ to its side[14], which was a Radiometer Physics RPG-MWSC-160 ($1864\mu m$). Then, both signals sampled at $1kHz$ including a GPS timestamp were send to a local computer. For the validation we used CESAR's EC measurements at $3m$ height ($10Hz$). Furthermore, we used CESAR's net radiation ($Qnet = S_{in} - S_{out} + L_{in} - L_{out}$[15]) and ground heat flux (G) to close the surface energy balance. For additional validation on evapotranspiration we used data from an Eikelkamp SMART-Lysimeter

[14]The mounting points at the transmitter and receiver cite were swapped, this makes their path's cross in the centre (like in Figure 1), thus ensuring that (approximately) the same eddies were observed

[15]Here, S = shortwave radiation, L = Longwave radiation

recently installed at CESAR. We focused on the period from September 8^th 2020 up to and including October 9^th of the same year as all measurement devices were operational in this window.

z_0 at CESAR

The scintillometry method requires a well defined z_0. Beljaars and Bosveld (1997) defined WD dependent roughness lengths for the Cabauw site. However, z_0 varies with changes in the environment like extra obstacles or roughness caused by plant growth. As the values in the paper might be outdated, we calculated our own. We did this by solving equation 15 for z_0. u_* itself can be solved from EC directly with equation 21 displayed below.

$$u_* = \sqrt{-\overline{u'w'}} \tag{21}$$

Note that inverting equation 15 can not be done analytically and thus requires an iterative procedure. Furthermore, z0 is only well defined at larger values for u_* (thus windspeed). Consequently, we only used data where $u_* > 0.2$. Figure 15 displays all resulting z0 values, including the way we categorized them dependent on their WD.

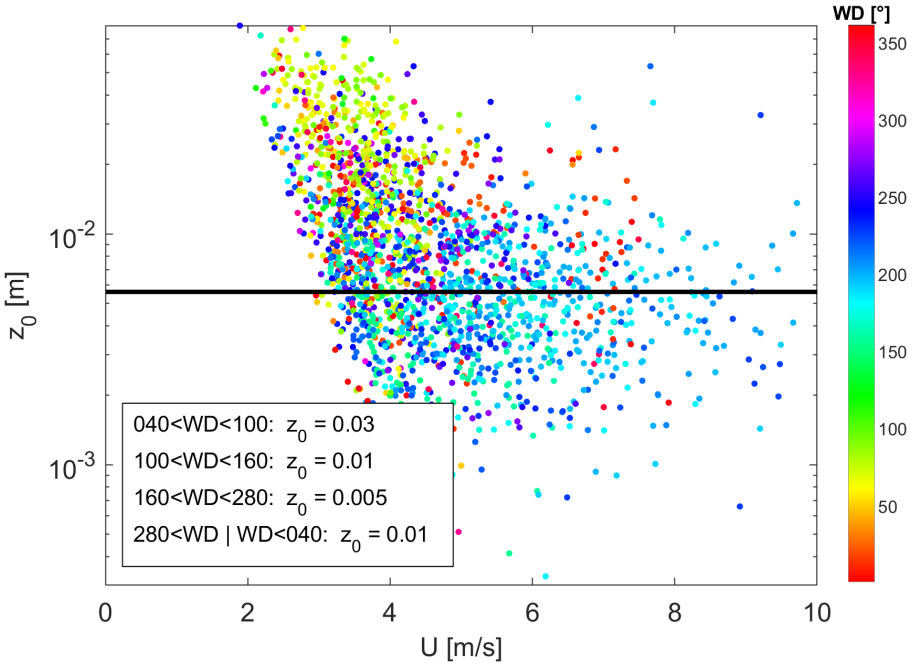

Figure 15: z_0 values determined with EC by solving for z_0 in equation 15. The black line represents the z_0 values over the entire domain. We assigned WD dependent clusters in the figure to the approximate z_0 value they resemble.

5 Results

The results are structured based on the validation methods we have used. First, we will compare scintillometry and its various processing methods to the EC measurements. Afterwards, we will show the results from our LES, including a direct comparison between virtual and real scintillometer measurements. Finally, we will use lysimeter and net-radiation measurements to get another perspective on our scintillometers output.

5.1 Scintillometry versus Eddy Covariance

In this subsection we compare our scintillometer results in detail to the EC measurements. First, we focus on the fluxes, and consequently on the structure parameters. Along the way, we visualize the influence of the roughness length (z_0), MOST coefficients, wind direction (WD), and entrainment. All data in the figures are based on 10-minute data intervals ($N = 4608$) unless otherwise specified.

5.1.1 Optimal method for processing scintillometer data

In order to decide which method for processing scintillometer data performs best we compared their respective outputs with Eddy Covariance. Here, we used the MOST coefficients defined by Kooijmans and Hartogensis and z_0 from our own EC measurements (see table 2 and figure 15 respectively). The time-series from an example day are displayed in figure 16.

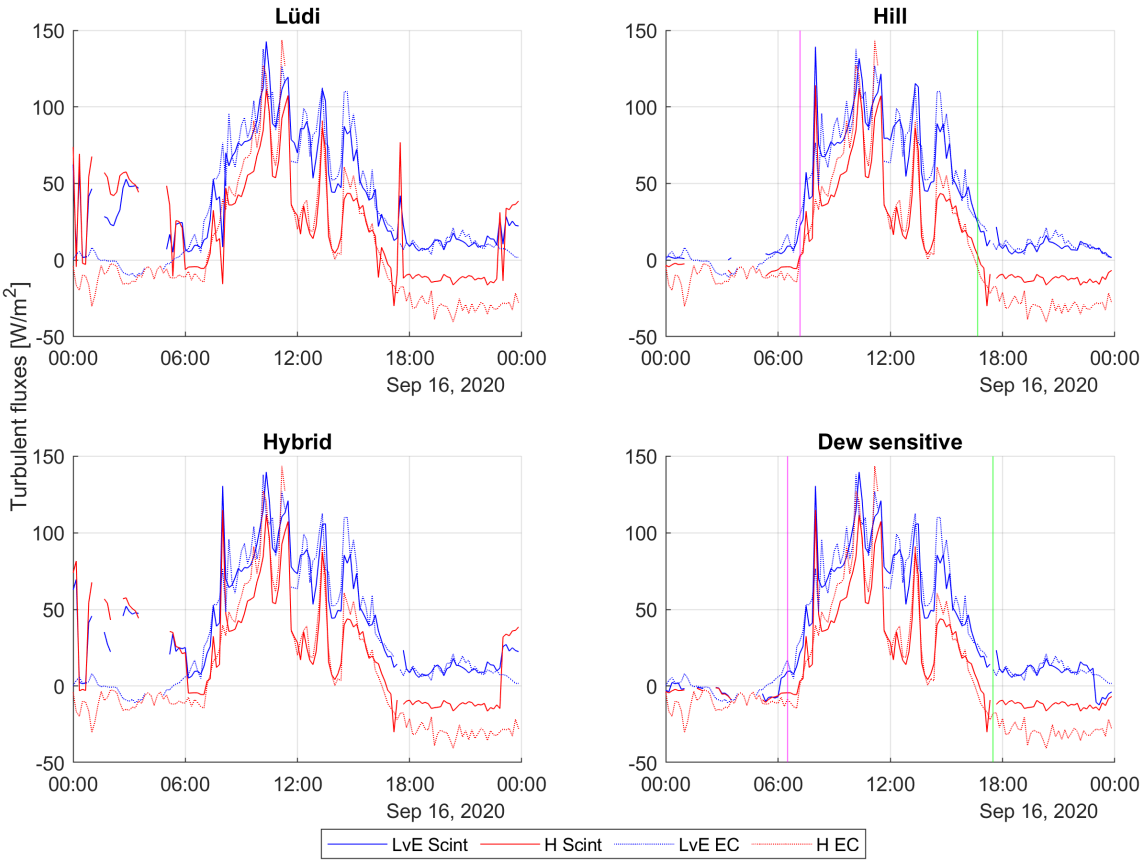

Figure 16: Time-series comparing the scintillometer methods. Scintillometer fluxes were calculated with: MOST coefficients from Kooijmans and Hartogensis and WD dependent z_0 from EC data. The pink and green lines represent the Hill and dew detecting methods transitions (see sections 3.1.4 and 3.1.5).

According to figure 16 there is large agreement between all scintillometer and EC outputs on the general trend in - and magnitude of - the daytime fluxes. Jumpiness in the sign around the morning and afternoon transitions is exclusive to the Lüdi method. The EC output suggests these fluctuations are incorrect. The biggest discrepancy between the scintillometer methods occurs in the early morning, where the Lüdi and Hybrid methods observe unstable conditions. It is clear from the Eddy Covariance method that conditions were in fact stable. The only method able to reproduce the early morning dew is the dew detecting method. The Hill method was not able to resolve any fluxes in the early morning. Also, note that the order of magnitude of the scintillometers night-time H is too small compared to EC. This same pattern can be seen in the figure 17.

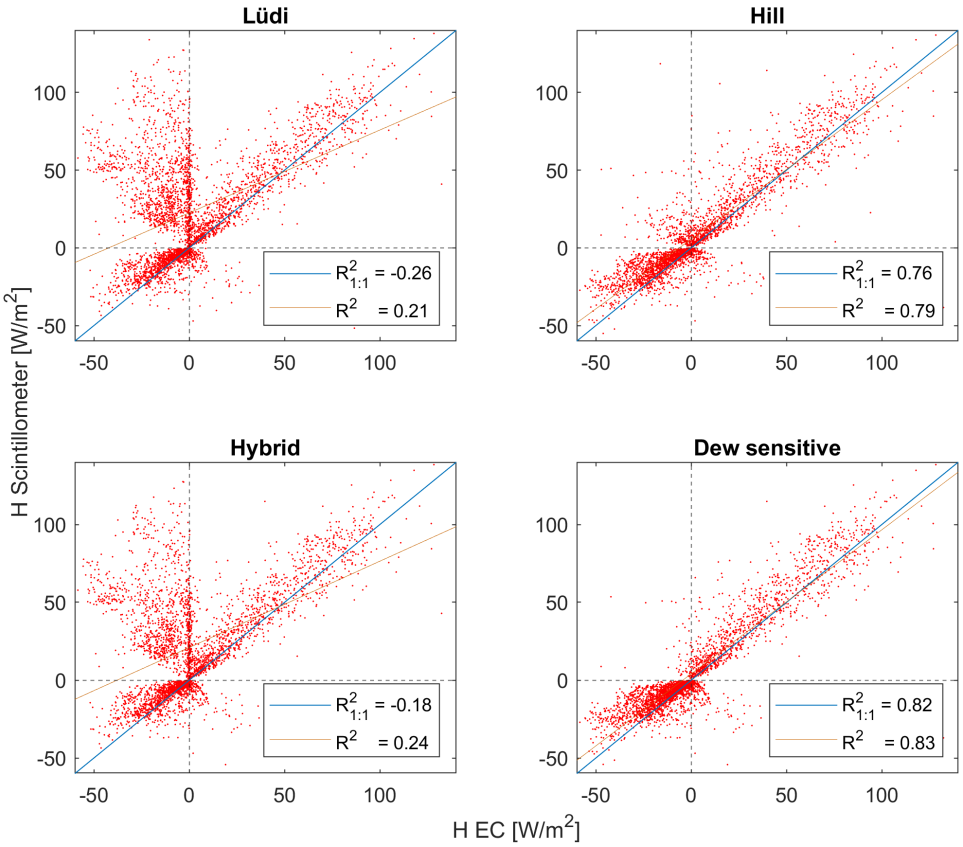

Figure 17: Scatterplots between EC and scintillometer methods. Scintillometer fluxes were calculated with: MOST coefficinets from Kooijmans and Hartogensis and WD dependent z_0 from EC data. The negative values for $R^2_{1:1}$ indicate that H from scintillometry can better be predicted by its average then by H EC.

Figure 17 shows the relations between the H of the various scintillometer methods and EC over the entire measurement period. The underestimation of H during stable conditions results in an angle between the scattered dots and the 1:1 line, best visible in the Hill and dew detecting methods. The Lüdi and Hybrid methods suffer from considerable sign errors during stable conditions, resulting in the plumes in the top left of their figures. During daytime (positive H EC) all scintillometer methods correspond well EC, like we saw in figure 16.

Similar to H the daytime values for LvE from the scintillometry methods and EC correspond well (see figure 18). However, there is significantly more scatter around the 1:1 line for this turbulent flux. Again, the Lüdi and Hybrid methods suffer from sign errors, mis defining small and negative latent heat fluxes as large and positive. Note that the dew detecting methods is making a similar but opposite error. Here, the r^2 statistic reveals that the misclassification

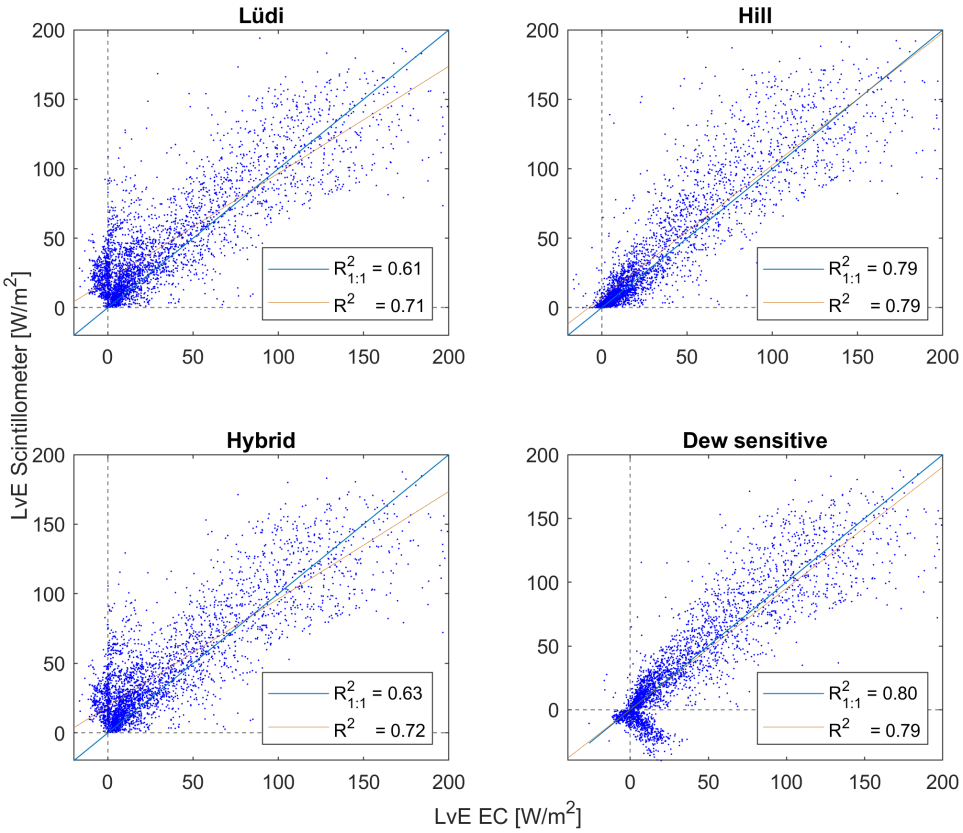

Figure 18: Scatterplots between EC and scintillometer methods. Scintillometer fluxes were calculated with: MOST coefficients from Kooijmans and Hartogensis and WD dependent z_0 from EC data.

by the Lüdi and Hybrid methods is significantly more damaging to their overall results. One reason is that part of the negative effects caused by sign errors in the dew detecting method are compensated by correct classifications of dew events. Overall, the dew detecting method was most similar to EC in terms of both H and LvE. This meant it was the method we used for our further analyses.

5.1.2 MOST optimization

Optimizing the MOST coefficients strengthens the relation between the scintillometer and EC methods in clearly visible - like correcting the magnitude of the sensible heat flux during stable conditions - and hardly visible ways. While optimizing MOST coefficients, we had an additional opportunity to test which set of wind dependent z_0's performed best. We did this by performing two separate

optimizations with either set of z_0's. The outcomes can be seen in figure 19, and their respective coefficients are found in table 5.

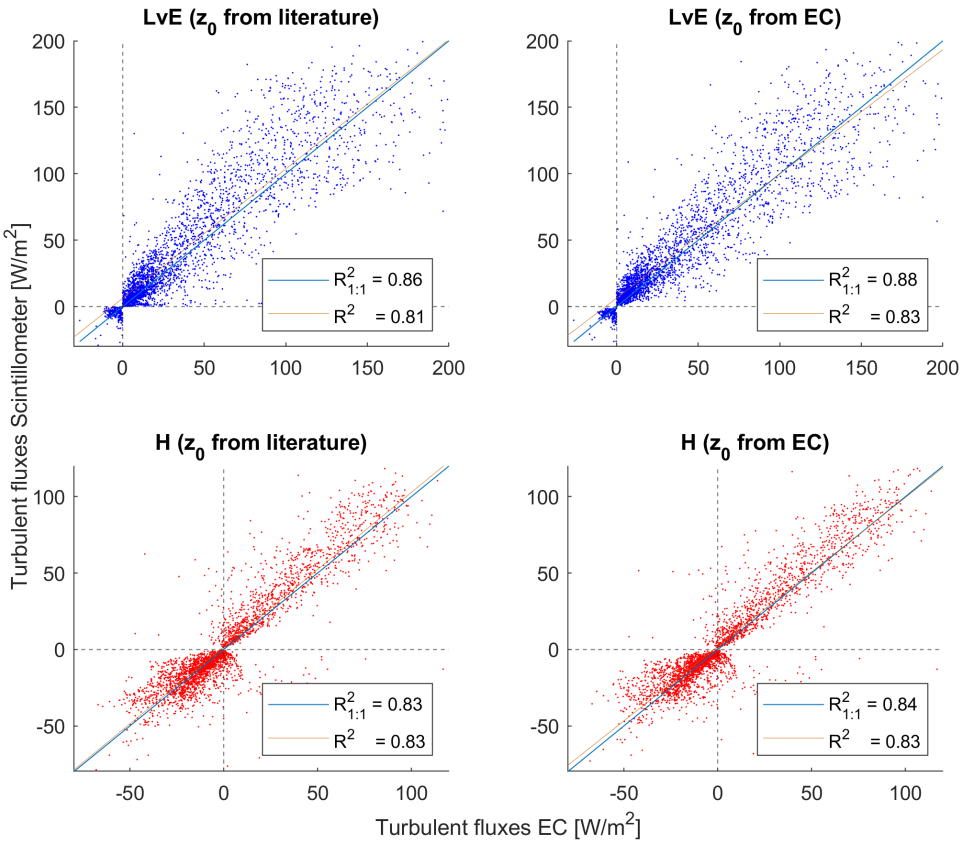

Figure 19: Scatterplots to compare z_0 effect. Scintillometer fluxes were calculated with: MOST coefficients from table 5. Here, that the sign of LvE from scintillometry is determined by LvE EC, as this is how the MOST coefficients are optimized [16]. z_0's from literature come from Beljaars and Bosveld (1997).

It is clear from figure 19 that after optimization, agreement between EC and scintillometry has improved. Note that we used the the sign of the EC LvE for the scintillometer LvE to prevent sign errors influencing the MOST optimization, like explained in the methods section. While this explains part of the improved relation for LvE, the scatter around the 1:1 line has also been reduced as can be seen from H. When comparing the various z_0's in figure 19, the variant form EC performs better with respect to LvE and H. Still, the spread in LvE during unstable conditions (positive fluxes) is substantial.

Table 5: MOST coefficients determined by our MOST optimization scheme for the two variants of WD dependent z_0. Colors indicate similarity to margins around general coefficients by Kooijmans and Hartogensis. Green; within margins, yellow; near margins, and red; not near margins.

Optimized MOST coefficients	z_0 Literature		z_0 EC	
Unstable conditions ($\zeta < 0$)	$f_{C_T^2}$	$f_{C_q^2}$	$f_{C_T^2}$	$f_{C_q^2}$
c_1	6.5	6.0	6.2	5.7
c_2	7.3	14.0	8.0	13.3
Stable conditions ($\zeta > 0$)	$f_{C_T^2}$	$f_{C_q^2}$	$f_{C_T^2}$	$f_{C_q^2}$
c_1	6.3	6.0	4.0	6.0
c_2	0.0	4.9	0.0	0.0

5.1.3 Reducing spread in LvE

Investigation into the spread in LvE revealed that scintillometry overestimated LvE during certain days, while underestimating the same flux on other days. To find out which variable influenced this variability we compared the daily averaged discrepancy in LvE between scintillometry and EC, defined as $dLvE = \overline{LvE_{Scint} - LvE_{EC}}$, to the daily averages of other key meteorological variables. Here, we limited ourselves to unstable conditions.

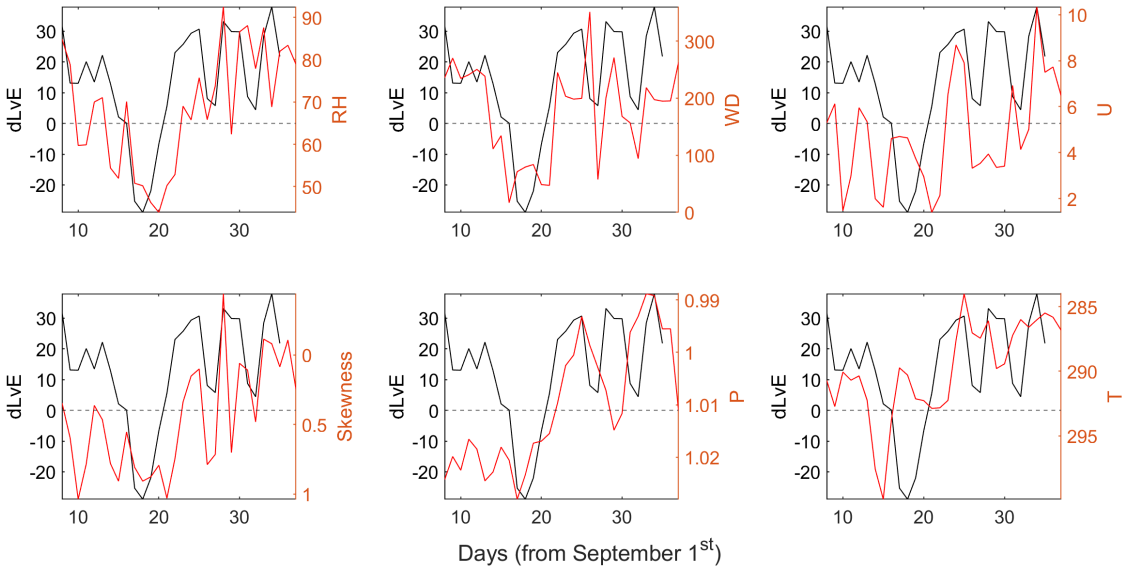

Figure 20: Trend in dLvE over the days compared to various meteorological variables. Note that the y-axes of $Skewness$, P, and T are inverted.

In figure 20 we only plotted those meteorological variables which seemed to have some correlation with $dLvE$. However, it is clear that no individual meteorological variable dominantly explains the variability in $dLvE$. Instead, it looks like $dLvE$ is dependent on the weather conditions. As a whole The dip in $dLvE$ around day 18 corresponds to a high pressure area with warm, dry air and a deep convective boundary layer (as indicated by the skewness[17]) coming in from the East (land). Around day 30, The opposite situation occurs with wind coming from the West (sea). We found that when looking at 10-minute intervals instead of daily averages, the WD was best able to separate out the weather regimes. Consequently, we split the data based on three WD regimes and applied MOST optimizations to all of them separately (coefficient in Appendix B table 6). The effect of this is displayed in figure 21.

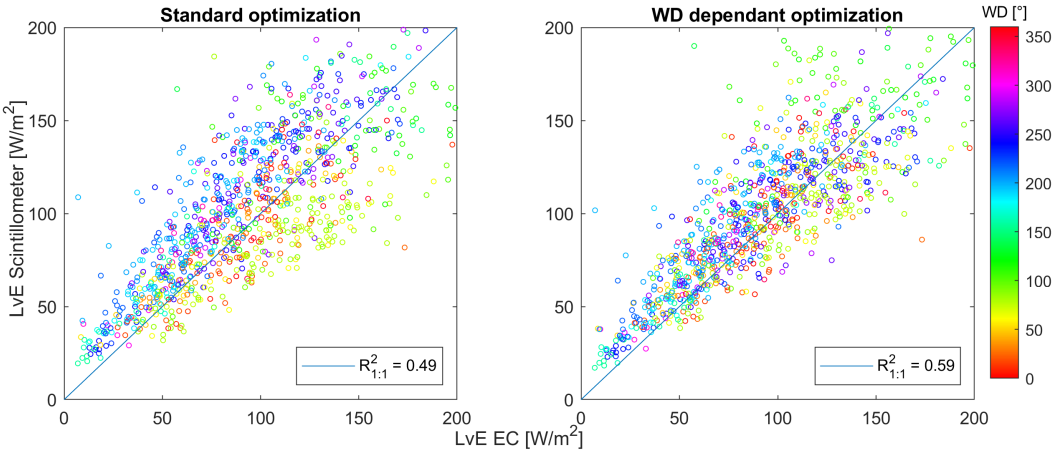

Figure 21: Scatterplots to compare MOST optimizations. Scintillometer fluxes calculated with: z_0 from EC data, standard optimization uses coefficients from table 5, WD dependent coefficients in Appendix B, table 6. Note that only the intervals taken during unstable conditions are displayed.

From figure 21 it follows that WD dependent MOST optimization reduced the impact of WD on the spread in LvE. Consequently, the relation between the LvE from EC and scintillometry has improved. As the influence of WD on the spread in H was significantly smaller, the spread in H hardly improved (figure 30, section 6.1.1). The $R^2_{1:1}$ values between the fluxes of EC and this final scintillometer optimization were 0.84 for H and 0.84 for LvE (figure 38, Appendix B). In the following subsection we use these scintillometer fluxes to look into the effect of entrainment on LvE.

[17] We will expand on how this works in the discussion section about entrainment tracers.

5.1.4 Entrainment tracers

During entrainment events, MOST is known to be violated which causes scintillometry to overestimate LvE. We used the skewness of q and a quadrant analysis of LvE flux to investigate the effects of the entrainment of dry air (see section 3.4). We classified the skewness values into tree modes. Here, strong entrainment is defined as $skewness < \frac{1}{3}$, medium entrainment as $\frac{1}{3} < skewness < \frac{2}{3}$, and light entrainment as $skewness > \frac{2}{3}$. For the quadrant analysis such categorization was not applied as its magnitude can be interpreted as the magnitude of entrainment itself. We visualized the impact of entrainment on our fluxes in figure 22.

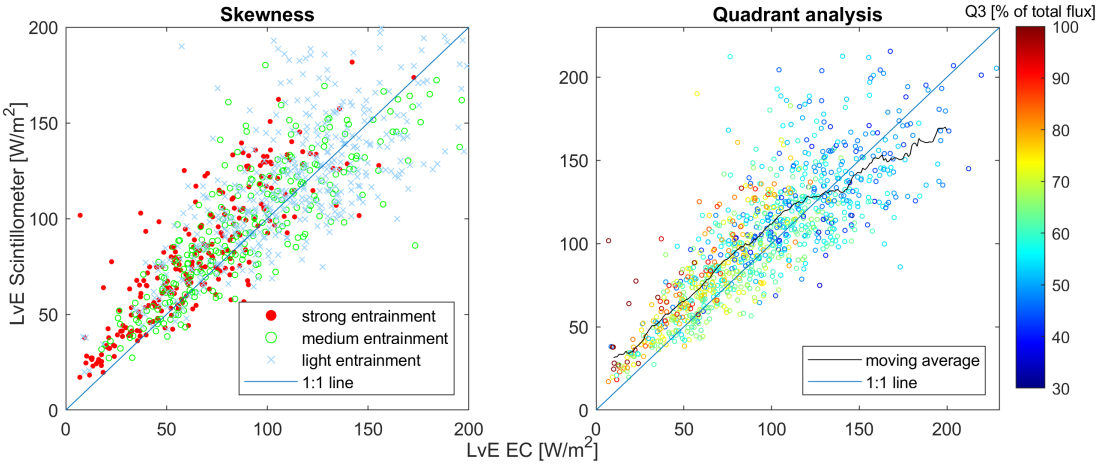

Figure 22: Scatterplot indicating entrainment effects. Scintillometer fluxes calculated with: WD dependent MOST coefficients and z_0. Furthermore, the moving average uses a window of 20 $\frac{w}{m^2}$.

Both plots in figure 22 show that the scintillometer generally overestimates the LvE flux during entrainment events. This suggests that entrainment impacted the scintillometers LvE through MOST. Furthermore, it seems like entrainment does not occur at large latent heat fluxes. Since the MOST optimizations was done with the effects of entrainment included, large latent heat fluxes which were not influenced by entrainment seem to be underestimated with scintillometry (see the moving average).

To better understand this behaviour we can look at figure 23. Here, we plotted the diurnal pattern of the skewness (thus including stable conditions). During night-time, skewness tends to be small. This is because no convective boundary layer is present to prevent dry pockets of air from the free troposphere to reach the surface[18]. However, no significant LvE fluxes occur during such conditions anyway. When the sun is at its peak, the convective boundary layer is deep and still growing, making it hard for tropospheric dry air to reach the surface. Consequently, entrainment is only able to significantly alter LvE through MOST during the development and destruction of the convective boundary layer. This is in line with the observations from figure 22 and can also be seen in the LES data (not shown). It is clear that MOST is a weak spot in the scintillometry method. Herefore, we continue with a comparison between scintillometry and EC based on structure parameters.

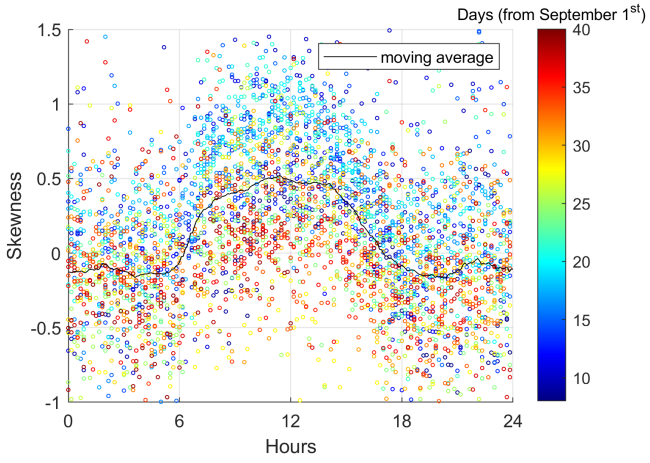

Figure 23: Daily trend in skewness. Moving average window is $1.8h$. Note that colors represent days.

5.1.5 Comparison with EC structure parameters

In the previous section we showed that the dew detecting method corresponds best to EC. We will therefore use the Hybrid methods structure parameters (used by the dew detecting method) for comparison with EC. Furthermore, we use the structure function based and spectra-based structure parameters for EC as discussed in the methods section. The main purpose of this analysis is to compare scintillometry with EC without any influence from MOST. Consequently, we used a simpler approach to scale the structure parameters using their measurement height ($*z_{eff}^{2/3}$). Figure 24 displays the relationship between the structure parameters (including r_{Tq}) from the spectral EC method and scintillometry.

[18]We explain how the skewness of q is influenced by tropospheric dry air in the methods section

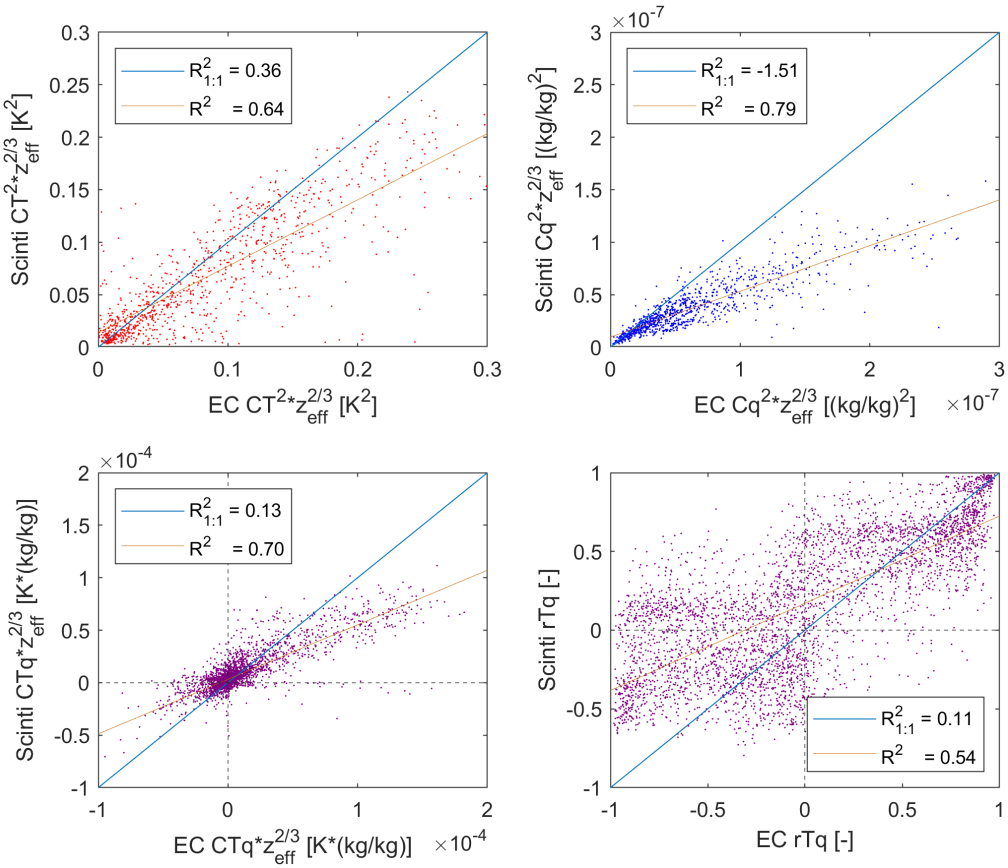

Figure 24: Comparison between EC and scintillometry on structure parameter level. Here the EC structure parameters were calculated with spectra.

We can see from figure 24 that there is a discrepancy in the magnitude of the structure parameters between scintillometry and EC. Those measured by the EC method are consistently larger. Furthermore, the spread in C_q^2 is significantly smaller then in C_T^2. This is opposed to the pattern seen in the fluxes (e.g. figure 19). Note that for the C_T^2 and C_q^2 we only display the structure parameters under unstable conditions as severe scatter occurs during stable conditions. The pattern in r_{Tq} is surprising, as a linear trend was expected. Instead, it seems like the scintillometer was more consistent in it's r_{Tq} value resulting in the horizontal lines. Also, there is significant disagreement between the methods about the sign of r_{Tq}. This might be related to the sign errors observed in the LvE of the dew detecting method (see discussion). Figure 39 (Appendix B) displays the same figures only then for the EC structure function method. Here, the difference in the magnitude of the structure parameters is even larger. Interestingly, the ones measured by EC are consistently smaller in this case. It

does seem like the spread in C_T^2 is smaller for the structure function method then for the spectral method. However, this is partially caused by the slope of the trend. The pattern in the r_{Tq} plot is nearly identical to the pattern observed in figure 39. In the next section we will discuss the LES outputs and get another look at the discrepancy between the spectral and structure function methods for determining structure parameters.

5.2 Scintillometry versus Large Eddy Simulation

In this section we start with a comparison between the structure parameters derived from 'virtual' and 'actual' scintillometry. Hereafter we make a similar comparison with respect to the fluxes, including those in the footprint of the scintillometer (according to the LES). Again, all data presented are based on 10-minute data intervals.

5.2.1 LES structure parameters

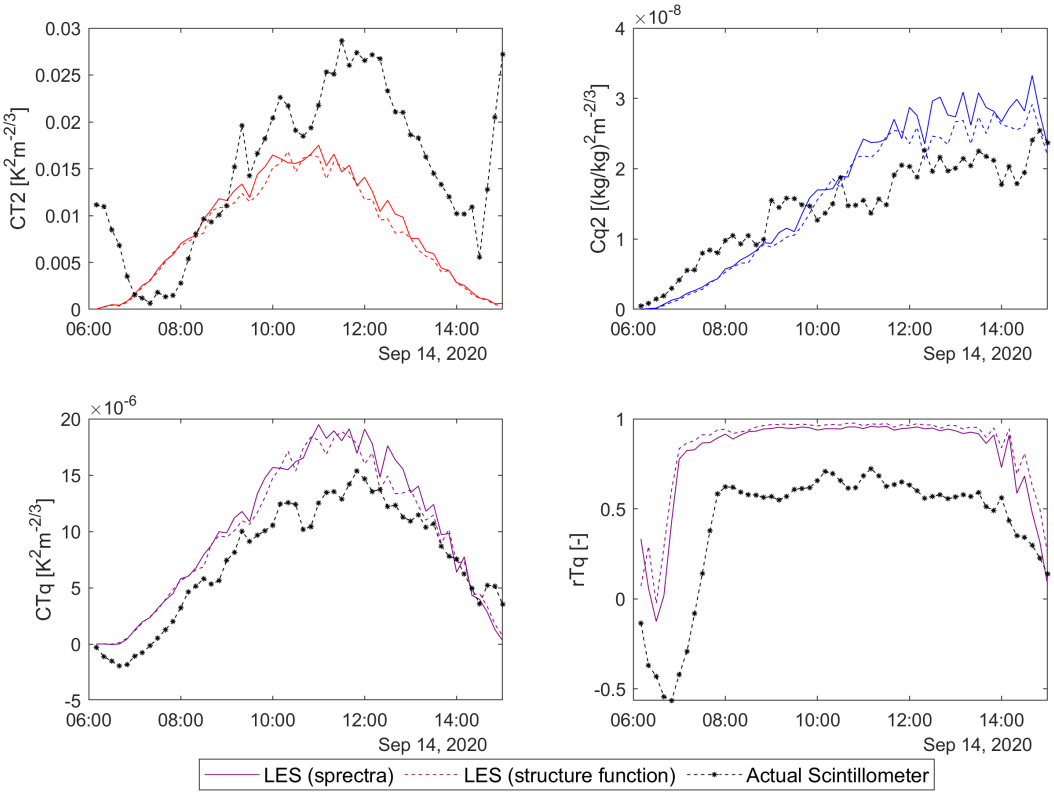

Figure 25: Comparison between virtual and real scintillometry on structure parameter level, all measured at ∼10.5m height. Thus, we omitted scaling.

The time-series of the structure parameters (including r_{Tq}) over the entire duration of the LES are displayed in figure 25. As you can see, the spectral and structure function methods of determining the structure parameters within the LES give near identical outputs. This is in sharp contrast to the outputs from both methods using EC data, which differed greatly (figures 24 and 39). The correspondence with the actual scintillometer is reasonable but has some noteworthy differences. Firstly, there is a phase shift of $\sim$ 1.5h in C_T^2 during both the morning and afternoon transitions. This phase shift seems to be inverted and not as large for C_q^2. Note that the final values from the actual scintillometer are compromised as they should have been stable (negative H) instead of unstable. Secondly, the actual scintillometer has significantly negative values for C_{Tq} and r_{Tq} in the early morning while the virtual scintillometer does not. Finally, the r_{Tq} from virtual scintillometry is close to its theoretically expected value of $|1|$ during daytime, while the actual scintillometer remained at 0.6.

5.2.2 LES fluxes

Comparing the turbulent fluxes themselves is the ultimate test to see how similar virtual scintillometry is to actual scintillometry. However, be aware that the roughness lengths (z_0) used in the determination of u_* (and thus the flux calculation) were different for the virtual and actual scintillometer measurements (see methods). Furthermore, we used the WD dependent MOST coefficients for the actual flux calculations while using 'the standard optimized coefficients' (right column table 5) for the virtual fluxes[19]. The resulting fluxes are displayed in figure 26.

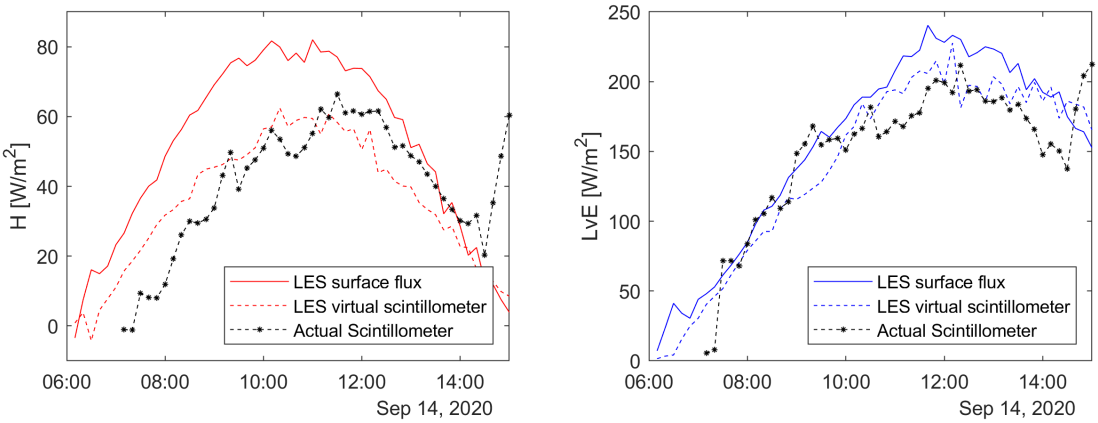

Figure 26: Comparison between virtual and actual scintillometry fluxes. Note that the actual scintillometry values after 14:30 are compromised

[19]We did test other MOST coefficients for virtual scintillometry like those from Kooijmans and Hartogensis (table 2) and the left column of table 5. However, the standard optimized coefficients resulted in fluxes most similar to the surface fluxes.

When looking solely at the LES outputs in figure 26 we see good correspondence between the surface fluxes and the virtual scintillometer fluxes. The underestimation of H by virtual scintillometry is the only significant deviation. The phase shift in actual scintillometry compared to virtual is similar to what we observed in the structure parameter comparison. However, in this case there is no clear time shift in H during the afternoon transition. The magnitude of the turbulent fluxes does correspond well between actual and virtual scintillometry.

5.3 Scintillometry versus Lysimeter and the surface energy balance

So far, our analysis have been limited to comparisons with EC, either directly or indirectly through MOST. As EC is suspected of flux underestimation (e.g. Schalkwijk et al., 2015), we used lysimeter and net-radiation data to get additional validation on the magnitude of LvE and the sum of the turbulent fluxes.

5.3.1 Lysimeter water balance

Lysimeters measure evapotranspiration (ET) through the weight loss of a part of the land surface (vegetation + soil) contained in a metal bucket. The lysimeter data we used provided such measurements at 1h intervals. Figure 27 displays two example days in which LvE from Scintillometry is compared to that of the lysimeter.

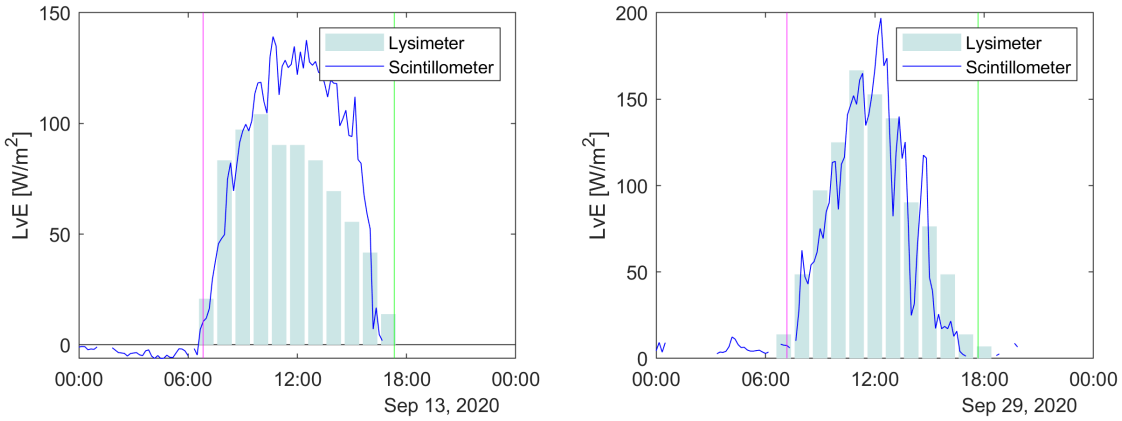

Figure 27: Comparison between lysimeter and scintillometer LvE on two example days. Scintillometer fluxes calculated with: WD dependent MOST coefficients and z_0 from EC data

From figure 27 we can see that there is a clear discrepancy in the magnitude of LvE on the 13^th, but not on the 29^th. This discrepancy is not in line with the expected underestimation of the scintillometers flux. Furthermore, the lysimeter flux is skewed to the left on the 13^th with respect to the scintillometer

flux. This gives us insight into the hydrometeorological situation that day. The scintillometer and EC (not shown) indicate dewfall in the early morning. After sunrise, the water evaporated from the wet vegetation but after this water was gone the lysimeter started underestimating LvE. According to Fred Bosveld (KNMI), responsible for CESAR's continuous measurements, this is because the grass in the lysimeter was not alive at this point. The reason why LvE was not underestimated by the lysimeter on the 29^{th} can be derived from the daily ET sums displayed in figure 28.

Figure 28 indicates the daily lysimeter and scintillometer ET sums, and how it was impacted by precipitation. We ignored dewfall by only summing positive LvE events. Furthermore, to prevent underestimation of this sum caused by data gaps, we applied linear interpolation to our scintillometer signal. The figure indicates underestimation of the lysimeter fluxes during the first half of our measurement period. From the 23^rd onwards it started to rain regularly causing the lysimeter to evaporate relatively more water. Inspection of the daily lysimeter ET trends showed unrealistic behaviour during this period, which explains the irregularity between the lysimeter and scintillometer ET sums[20].

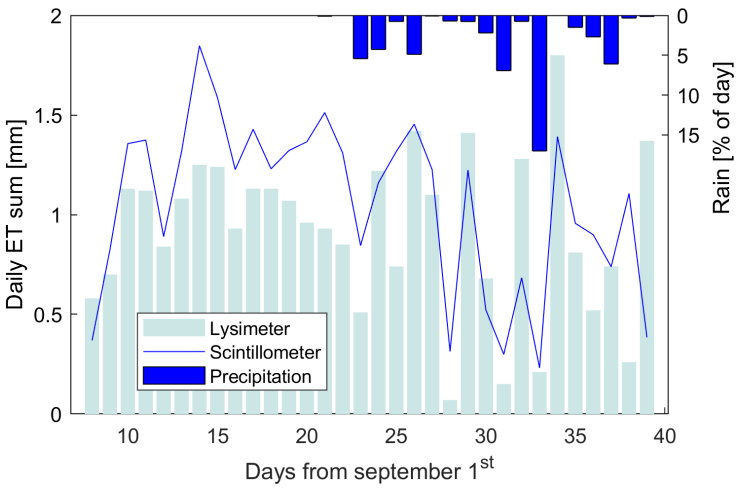

Figure 28: Comparison of daily lysimeter and scintillometer ET sums. Scintillometer fluxes calculated with: WD dependent MOST coefficients and z_0 from EC data. Precipitation data is based on the scintillometers rain indicator as the lysimeter erroneously observed rain every day.

[20]The scintillometer fluxes are also less well defined during this latter period due smaller, more variable fluxes and data filtering.

5.3.2 Energy balance closure

The surface energy balance can be separated into a turbulent $(H+LvE)$, radiative, (Q_{net}) and soil heat flux (G) part. By comparing $Q_{net} - G$ to $H + LvE$ we can see if all energy is accounted for. Note that G is defined as positive when energy is going into the soil. Figure 29 indicates how well the energy balance closed during our measurement period.

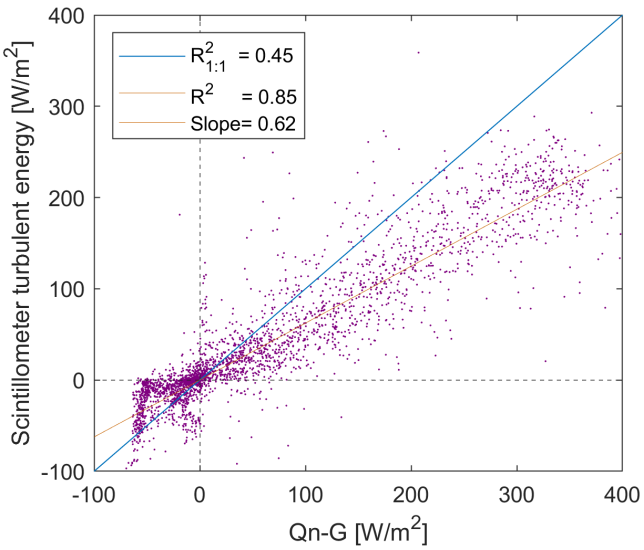

Figure 29: Comparison between available energy and the measured turbulent energy. Scintillometer fluxes calculated with: WD dependent MOST coefficients and z_0 from EC data. The trendline was forced through 0,0.

It is clear from figure 29 that the total turbulent energy is nearly always smaller then the total available energy during daytime. The scintillometer seems to react less to variations in energy availability between 0 and $40\frac{W}{m^2}$. At night, the scintillometer fluxes only become significantly negative when the energy deficit at the surface is large enough. In general, slope of the trendline indicates that the turbulent fluxes as measured with the scintillometer are 38% smaller then would be expected from the available energy. In Appendix A we explain a hypothesis we came up with, which suggests a possible cause for the structural underestimation of the turbulent fluxes.

6 Discussion

We organized our main discussion points along four themes. First, we will discuss those that have to do with scintillometry itself. Secondly, we discuss those related to the dew detecting method. Finally, we will consider some discussion points that came up during our research which are related to scintillometry.

6.1 Measurement site

6.1.1 Footprint differences

One of the fundamental assumptions during our research has been that the footprints of the scintillometer and the EC-system overlap in such a way that the average fluxes in their footprints are identical. However, there is an argument to be made that while the CESAR cite is very homogeneous, wind from the north and east could result in footprint differences (see figure 14). This would largely be due to the higher z_{eff} of the scintillometer compared to the EC-system resulting in a longer footprint. Since we do observe a WD effect on the discrepancy between scintillometry and EC, this hypothesis is worth discussing. According to figure 21, northerly and easterly winds cause the scintillometer to underestimate LvE.

This is in line with the urban land-uses to the north and east which have larger Bowen ratios ($\frac{H}{LvE}$). Another feature of roads and buildings are the larger albedo values compared to grasslands, which theoretically give them more total turbulent energy. Herefore, if significant footprint differences did occur during northerly and easterly winds, we would expect the scintillometer to strongly overestimate H during these conditions. Figure 30 shows how the relation between EC and scintillometry is influenced by WD. Instead of an overestimation in the scintillometers H

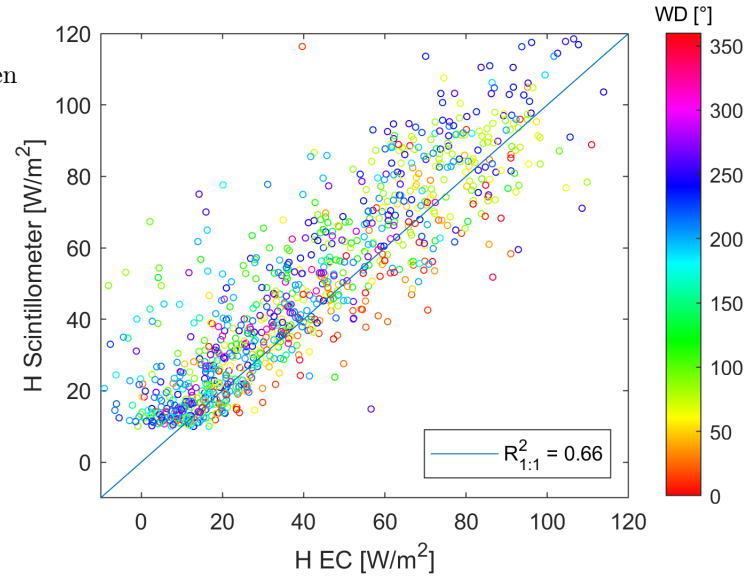

Figure 30: Scatterplots to see WD dependence in H. Scintillometer fluxes calculated with: z_0 from EC data and coefficients from table 5.

during northerly and easterly winds, figure 30 shows no overestimation or even a slight underestimation in H. Clearly, this is not in line with mismatching footprints and strengthens the case that different weather conditions associated with WD differences influence MOST instead.
Our footprint analysis of the surface fluxes in the LES (figure 10) gives additional insight into possible footprint differences. This is because we calculated the weighted average surface fluxes for both the scintillometer and the EC. Furthermore, the day that our LES simulated had predominantly easterly wind, which is the wind direction most apt to cause footprint differences. Figure 31 shows the time-series of H and LvE that day.

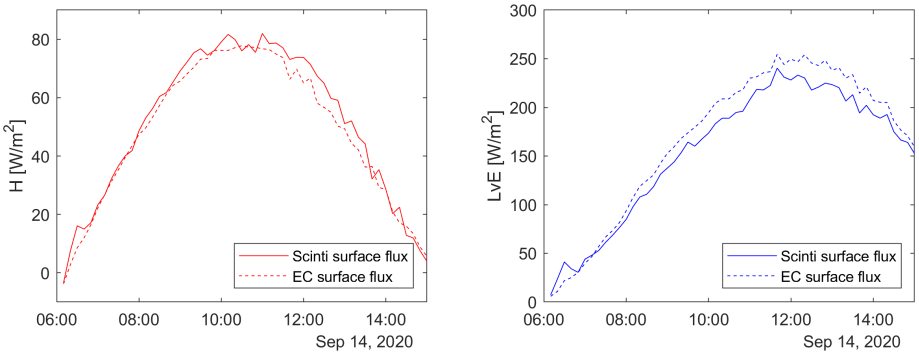

Figure 31: Comparison of weighted average surface fluxes in scintillometry and EC footprints.

It is clear from figure 31 that a discrepancy in the average surface fluxes is present. However, compared to figure 21, where WD dependent flux over and underestimations of 40% occur, the discrepancy is very small. Again, it seems like the strong WD dependence in the relation between EC and scintillometry has another cause then footprint differences. It should be noted that our LES used a constant albedo for the entire domain, potentially lessening the discrepancy surface flux. We don't expect a different concussion if albedo was included since the difference in the LvE surface flux would get smaller rather then larger and no WD dependence in albedo could be seen in the real measurements.
The last piece of evidence can be seen by comparing figure 24 to figure 21 (standard optimization). Both figures only show unstable conditions and indicate a measure for the spread in C_q^2 and LvE respectively. While the slope in figure 24 is clearly off, the spread in C_q^2 is much small then the spread in LvE in figure 21. As MOST is the only intermediate between the variables it is clear that it causes the spread and not a footprint discrepancy which would also have impacted the spread in C_q^2.

6.1.2 Weather conditions and entrainment

In the previous section we explained why weather conditions must be the cause of the under and overestimation's of LvE by scintillometry. One could argue that this is due to nothing but an increase in entrainment during days when the CBL is not well developed. Indeed, figure 20 indicates that the skewness clearly co-varies with the weather conditions, where tumultuous days have more entrainment (also see figure 23). However, even after we corrected for WD and thus for weather conditions, entrainment effects are apparent (figure 22)[21]. It seems that within each wind sector, strong entrainment events still cause the largest overestimation inLvE, which doesn't tell us much. Another important argument is that the split in $WD$is not limited to smaller values for LvE, where entrainment seems to have most influence on. Problematically, figure 23) does indicates that also during midday there was stronger entrainment on tumultuous days. It seems like we cannot definitively say whether the influence of the weather on MOST is caused merely by entrainment or also by additional changes in other atmospheric variables.

6.1.3 LES timeshift

The most striking feature from the comparison between the virtual and actual scintillometer fluxes is the $1h$ time delay in H of the actual scintillometer. While we are entirely sure what caused this, we know of two physical differences between the LES and the CESAR site which are likely to have had an effect. First off, while the LES surface has a land use related roughness, the obstacles don't have physical heights unlike reality. At the real CESAR site, shrubs and small threes are located to the east of the measurement site, where the sun rises. This could have caused shading resulting in a delay in the onset of the turbulent fluxes. Furthermore, we know that dew-fall occurred in the early morning of the 14^{th}, which the LES is not able to simulate. The evaporation of the morning dew can have caused the overestimation in LvE and underestimation in H with respect to the LES. However, these explanations do not account for the delayed peak in H of the actual scintillometer.

6.2 MOST optimization

The MOST optimization technique we applied in our research is somewhat unorthodox. To see if the resulting coefficients had realistic values, we compared them with the uncertainty range indicated by Kooijmans and Hartogensis (2016). The colours in tables 5 and 6 (Appendix B) indicate if the coefficients were inside, near (± 0.5), or outside the uncertainty range. We observe that our coefficients are generally not within the defined margins. Still, the magnitude of the coefficients tends to be in line with the theoretical ones. Furthermore, unstable and $f_{C_T^2}$ related coefficients tend to be closer to the expected value then the stable and $f_{C_q^2}$ related ones. This is in line with the observation by

[21] Note that without correcting for WD the entrainment effects were more pronounced

KH that $f_{C_T^2}$ is less variable between measurement sites and that unstable conditions tend to have more clearly defined coefficients. The fact that the c_1's are more similar to KH compared to c_2's is caused by the limited range of values we allowed c_1 to have. Clearly, our coefficients would not function well as universal MOST coefficients even though they could still be valid for the CESAR site[22].

During the optimization of H for wind directions between 50 and 150°. We could see that the stable coefficients related to $f_{C_T^2}$ were forced towards their lower limits, but unable to correct the relation between the Scintillometer and EC fluxes. Figure 32 visualizes this phenomenon. For the stable $f_{C_T^2}$, the lower the values of c_1 and c_2, the larger the magnitude of the negative sensible. Since we limited c_1 to a minimum of 4, c_2 gets minimized to 0.0 as it "tries" to reduce the angle in figure 32. Using MOST coefficients with negative values is no option as they are unrealistic and often result in imaginary numbers. Clearly there is some other element influencing on the relationship between H from EC and Scintillometry. z_0 is suspect as it is hard to define and has a direct impact on MOST. Furthermore, the values of z_0 at the CESAR site from Beljaars and Bosveld are an order of magnitude larger then the z_0 from EC which we ultimately used[23]. In line with this fact, larger values for z_0 do indeed improve the relationship between H from scintillometry and EC. However, it seems like the benefit gained by having a larger z_0 did not weigh up to its drawbacks according to our MOST analysis performed with both sets of z_0's (figure 19).

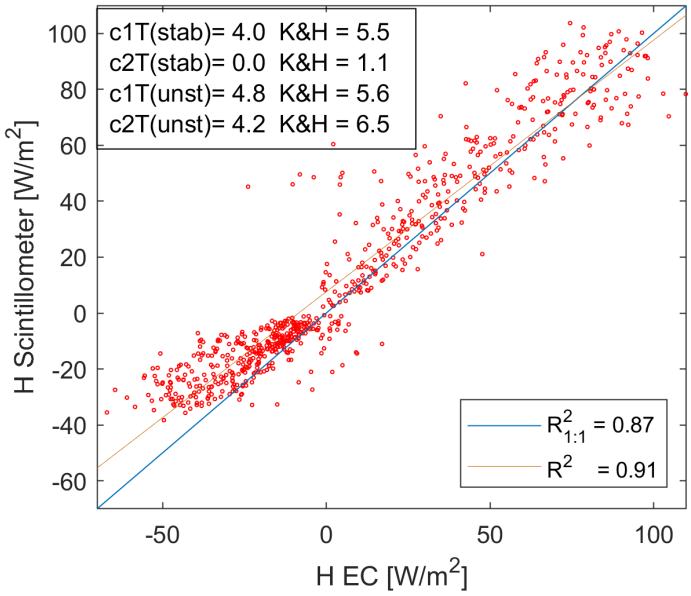

Figure 32: MOST optimization for $50<WD<150$. Scintillometer fluxes calculated with: MOST coefficients displayed in figure and z_0 from EC data.

Since a larger z_0 was not favoured, a more likely explanation of the discrepancy

[22]Be aware that our measurement period is relatively short, and therefore apt to influences from weather conditions (see figure 11). A longer measurement period should be used to define proper MOST coefficients.

[23]The actual effect of this order of magnitude difference is way smaller, as its impact is reduced by the $ln()$ term in equation 15

between H from EC and Scintillometry is that the scintillometer was disconnected from the surface layer due to its larger z_{eff}. Proof for such disconnection can be found in figure 29, which shows that scintillometry only responds to negative available energy when the energy deficit is significantly large. As this adequately explains why the scintillometer significantly underestimates the magnitude of the flux, we expect it to be the cause of the discrepancy and unrealistic MOST coefficients shown in figure 32.
We suggest a future experiment in which LES data is used to find MOST coefficients. Our research confirms that the magnitude of the fluxes between virtual and actual scintillometry can be expected to be similar. Clearly, the governing processes to resolve turbulence are adequately represented in LES. Also, a similar under closure of the energy balance can be seen from figure 26. Since LES explicitly solve the surface fluxes without interference from EC, it might be possible to find MOST coefficients which prevent under closure of the energy balance in the real word.

6.3 Scintillometry method

6.3.1 Convergence issues

The iterative procedure used to calculate fluxes with the scintillometer method has the tendency to converge to infinitely small values for the fluxes, u_{star}, and L_ob. This is due to the interaction between u_{star}, L_ob, and H and generally occurs during stable atmospheric conditions. As the stability is influenced by wind sheer, erroneous convergences occurred at low U's, with a mean of 1.4 and a standard deviation of $0.7\frac{m}{s}$. Figure 33 confirms this U dependence by showing that convergences to zero generally occur when $u_{star} < 0.15$. We chose our Bussinger-Dyer equation such that fewest convergence errors occurred[24](Beljaars and Bosveld, 1997). Still 15% in our intervals ended up with erroneous convergences. As extremely stable early morning dew conditions often converged to zero, the apparent effectiveness of the dew detecting method is limited. Tests in which we used u_{star} from EC didn't have any convergence issues and thus showed the true potential of the dew detecting method. Herefore, we feel it is important that new research is done to find a way to overcome convergence issues with scintillometry.

[24]As this practically comes down to generating large u_{star}'s this might explain the overestimation of u_{star} by scintillometry

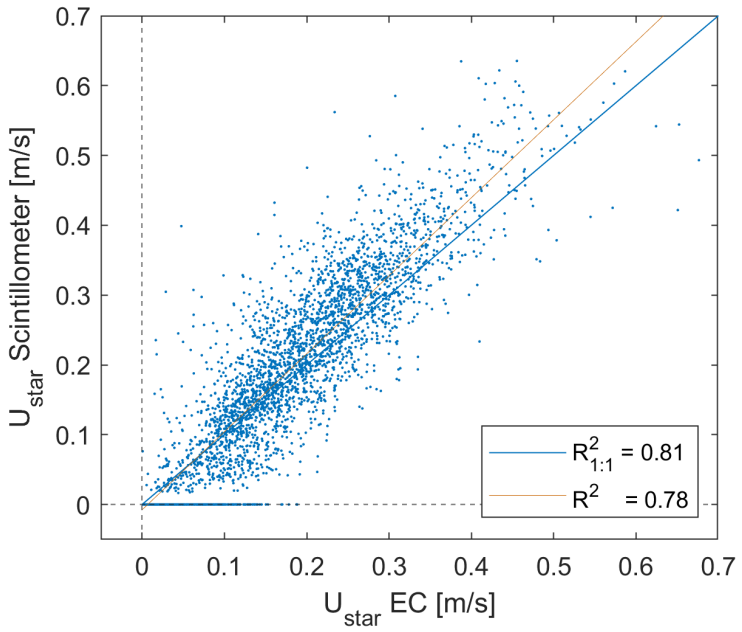

Figure 33: Comparing u_{star} from scintillometer and EC. Scintillometry u_{star} from equation 15, using Ψ functions from Holtslag and De Bruin (1988).

6.3.2 positive r_{Tq} during nocturnal conditions

Another key problem with scintillometry are false-positive r_{Tq}'s during nocturnal conditions. This causes all serious sign errors in our results (see figure 17 and 18). In the Lüdi and Hybrid methods it causes strongly unstable situations to occur in the middle of the night and in the dew detecting method it results in misinterpretation of LvE for dew-fall. One possible explanation could be the scintillometers disconnection from the surface layer causing its measurements to deviate from EC. However, while we have shown that MOST is seriously violated in such cases, the observed (anti)correlation between T and q (thus r_{Tq}) does not change. Instead, we suspect that noise in the scintillation signals of both the LAS as the MWS covary, and thus cause the positive r_{Tq}'s. Such noise is ever present in the scintillation signal, but has more influence at night as the 'real' signal gets relatively small (see section 3.2). Figure 34 shows LAS and MWS intensity spectra during a night where the sign of r_{Tq} was systematically wrong.

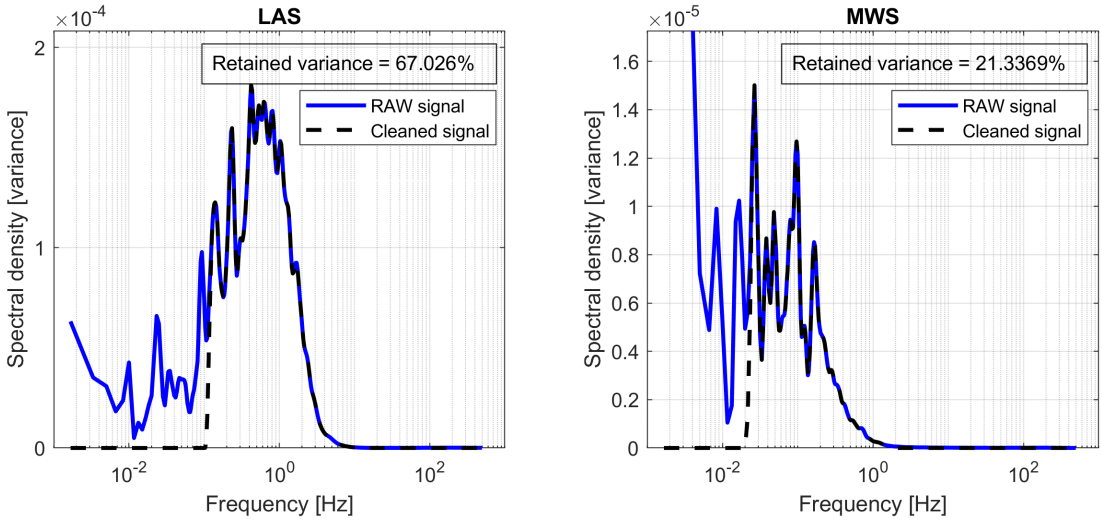

Figure 34: LAS and MWS spectra of a 10 minute interval between 03:40 and 03:50 on the 17^{th} of September 2020.

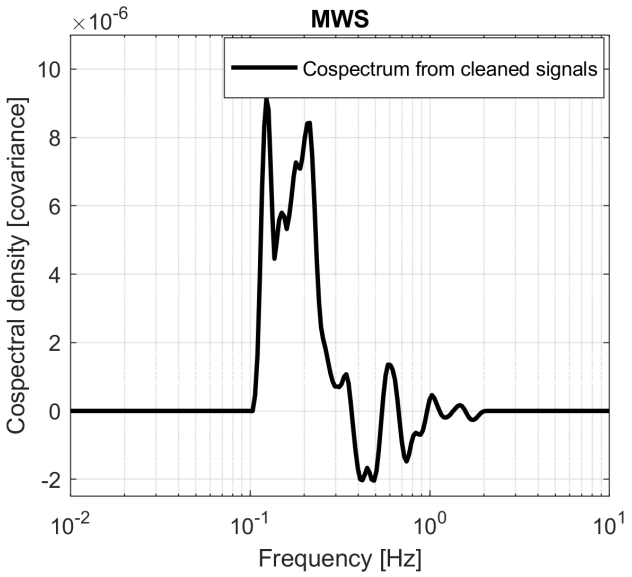

Figure 35: LAS and MWS cospectrum of a 10 minute interval between 03:40 and 03:50 on the 17^{th} of September 2020.

There is a clear influence of noise in the spectra in figure 34, which impacts the noise prone MWS more then the LAS. Furthermore, the noise is more pronounced at lower frequencies, like is generally the case. Figure 35 displays the cospectrum associated with the LAS and MWS spectra in figure 34. From this cospectrum we can see that the covariance between the scintillometer signals is indeed positive, suggesting a positive r_{Tq}. Furthermore, we can see that this positive covariance is caused by influences of the more noisy low frequencies instead of the cleaner high frequencies. This is perfectly aligned with the hypothesis we described above. It would

be interesting to see if some form of cospectral cleaning could prevent positive r_{Tq}'s caused by noise. Otherwise, a tool like the skewness might be applied to the LAS and MWS spectra to see if their shape is as expected. If their shape (and thus skewness) would be significantly altered by noise, the associated interval could be disregarded[25].
One other observation might help in reducing the sing errors in r_{Tq}. Figure 24 shows that true-positive and false-positive r_{Tq}'s have a structurally different value for r_{Tq}. The true-positives are aggregated around 0.6, while the false positives have values of approximately 0.2. When using 0.3 as the arbiter to decide the sign of the fluxes instead of 0.0, the number of sign errors will be significantly smaller.

6.4 Dew detecting method

For the CESAR cite, the dew detecting method worked best because dewfall occurred regularly. Yet, it is unclear if measurements over urban areas - where dew events hardly occur - would be harmed by using the dew detecting method. In urban areas, heat stored and emitted by buildings and roads can cause H and LvE to be positive until late at night. If this would be interpreted as dew by the dew detecting method, it would cause serious sign errors. However, it is expected that the afternoon dip in r_{Tq} regulating the mode transition (see section 3.2.5) of the dew detecting method would be delayed until late at night, still allowing for positive H and LvE throughout the evening. Furthermore, we observed deep drops in r_{Tq} during morning transitions when dew-fall did occur ($\sim$-0.5), while the drops associated with dew-less nights were less negative or even positive. This seems to be caused by the more intense inversion of the fluxes when transitioning between two modes with positive r_{Tq}'s. Also, the increased LvE caused by evaporation of dew sharpens the contrast with H and thus reduces r_{Tq} further. Figure 7 shows that the 18^th, on which false-positive dew-fall was observed, had a weak drop in r_{Tq} to -0.2[26]. Exploiting this feature could result in a scheme where the dew detecting methods does not change 'modes' during nights without significantly negative r_{Tq} during morning transitions. We expect that this, in combination with proper cleaning or filtering of noised induced positive r_{Tq}'s, could allow for the use of the dew detecting method over environments with only sporadic nights with dew (e.g. Urban) without resulting in serious sign errors.

6.5 Structure parameters

The results of the comparison between scintillometry and EC on the basis of structure parameters was somewhat underwhelming (see figures 24 and 39). The main cause of this was the severe scatter during stable conditions and the slopes of the point clouds with respect to the 1:1 line during unstable conditions. Here,

[25] The difficulty here is that higher frequencies have more data points. Possibly some log-transform could solve this.

[26] Also note the weak positive night-time r_{Tq} of 0.2 associated with noise in figure 7

the spectral method overestimated the magnitude of the structure parameters, while the structure function method (severely) underestimated them. The fact that the spectral and structure functions methods corresponded very well when applied to LES data indicates that some aspect unique to the EC methods must have caused the observed discrepancy. We do not expect the lack in averaging over space to have caused the different outputs between the methods since in principle this only influences scatter, not magnitude. Rather, we suspect that the Taylor approximation of frozen turbulence did not work as expected (equation 19). During our measurement period, only 1.4% of intervals had U_{avg}'s exceeding $10\frac{m}{s}$. Since our EC-system measured at $10Hz$, we think that our separation distance (r) of $1m$ can't have been the cause of this underestimation. Instead, wind gushes might 'artificially' have increased U_{avg} such that it causes underestimation of the value of structure parameters for the nominal eddies passing by. Furthermore, there is evidence in the literature that suggests that the Taylor approximation of frozen turbulence systematically underestimates the real height of the turbulent energy spectrum and thus the structure parameters (Cheng et al., 2017). Both could explain the underestimations associated with the structure function method applied to our EC data.
The cause of the systematic overestimation of the structure parameters from the spectral method (EC) compared to those from scintillometry remains unclear to us. Micro heterogeneities near the EC-system probably didn't inflate the structure parameters as we should see this back in the fluxes. A somewhat farfetched explanation can be derived from figures 25 and 26. They show that roughness differences between the actual and virtual measurement site can cause differences in C_T^2 which practically vanish in H as MOST corrects for z_0. Maybe, the increased footprint of the scintillometer did result in a significantly larger z_0, thus suppressing the structure parameters relative to EC[27]. Interestingly, a recent paper found a problem in the way we (and others) calculate structure parameters from power spectra (Gibbs and Fedorovich, 2020). They argue that a mistake was made in deriving equation 3, and that the value 4 should be replaced with an 8. Our results do not support their finding as even larger structure parameters from the spectral methods would worsen the relation between the spectral and structure function methods for our EC and LES data.

7 Conclusion

The goal during our research was to find out how reliable the vertical fluxes determined by LAS-MWS scintillometry are. We answer this question by briefly coming back to all separate research questions. Our validation with EC highlighted the problem of sign ambiguity in the scintillometry method (rq1). To counter this, we developed a new 'dew detecting' method for solving the sign. It is an extension of the hybrid methods and uses an additional bi-modal r_{Tq}

[27] Our LES does indicate an effect like this, but not at the magnitude which would explain the observed differences. Then again, its surface z_0 is a very course approximation of reality.

dependant scheme to separate cases with $+H$ and $+LvE$ from those with $-H$ and $-LvE$. The effectiveness of this dew detecting method was limited by false-positive r_{Tq}'s during nocturnal conditions with small values for r_{Tq}, probably caused by the covariance of noise between the LAS and the MWS.

We found that over and underestimation of LvE was linked to changes in weather conditions impacting MOST (rq2). By performing our own (WD dependent) MOST optimization, we were able to minimize this effect. The resulting coefficients differed significantly from universal ones and energy balance data partially explains these erroneous coefficients by suggesting that our scintillometer was regularly disconnected from the surface layer at night. Entrainment tracers indicated that entrainment was most intense during the development and destruction of the convective boundary layer and caused the scintillometer to overestimate LvE at such moments by violating MOST. Thus, while using LAS-MWS scintillometry at a reduced height might reduce the effects of entrainment and disconnection from the surface layer, they cannot be ignored.

From the various scintillometer methods we tested, the turbulent fluxes from the dew detecting method came closest to those from EC, even though convergence issues during stable conditions significantly reduced the number of data points on which the dew detecting method had an advantage (rq3). Our setup resulted in a $r^2_{1:1}$ between LAS-MWS scintillometry and EC of 0.84 for H and 0.84 for LvE. The key problems which should be addressed to increase this correlation are MOST non-universality (including entrainment), noise induced positive r_{Tq}'s, and disconnection from the surface layer.

Our validation with EC based on structure parameters indicates that it is not straightforward to compare scintillometry to EC without MOST (rq4). During stable conditions the structure parameters resulted in more scatter between the methods then was seen in the turbulent fluxes. Furthermore, the structure parameters from EC varied greatly dependent on the calculation method used, which we suspect was caused by the Taylor hypothesis of frozen turbulence. Additionally, decreased z_0 in the EC footprint might have resulted in the structural overestimation of the structure parameters with the spectral method. We were however able to verify that the relation in C^2_q showed significantly less scatter than the relation in LvE, supporting our claim MOST was non-universal and impacted by weather conditions.

With our LES we showed that virtual scintillometry measurements relate well to the surface fluxes in its footprint (rq5). Most notable was the underestimation of H compared to the surface flux. Since the surface energy balance in the LES was forced to close, this might be further evidence that real-life under closure of the energy balance is caused by EC (which impacts scintillometry through MOST). We suggest to optimizing MOST coefficients in a LES to prevent dependence on EC.

Finally, the turbulent fluxes from actual and virtual scintillometry correspond unexpectedly well (rq6). We did observe differences in structure parameters probably related to roughness differences and a time-shift which is likely to have been caused by evaporation of dew and shading on the real measurement site. Additionally, r_{Tq} in the LES is close to the theoretical value of $|1|$ while no

value larger than 0.7 is observed. Clearly *LES*'s resolve the dominant processes well but still differ from real life in the detailed aspects.

In general, state-of-the-art LAS-MWS scintillometry can be regarded as a robust method for determining spatially averaged turbulent fluxes at high temporal resolutions during unstable conditions. Here, the reliability of the magnitude of LvE is limited more by MOST then by entrainment of dry air. While we improved reliability during stable conditions, convergence issues, noise induced positive r_{Tq}'s, and disconnection from the surface layer seriously hampered the ability of our scintillometer to reliably resolve the turbulent fluxes.

Acknowledgements

I would first like to thank Oscar Hartogensis for his supervision. I greatly appreciate his many informative explanations and our discussions on practically all aspects of scintillometry. Here, I really valued his openness to my - sometimes unconventional - ideas. Also, a big thanks to Bart van Stratum, who was so kind to create the LES with microHH and answer my question about it. Finally I would like to thank Fred Bosveld for our discussion, for giving us access to the CESAR data, and for answering my questions about this data.

8 References

Andreas, E. L. (1988). Estimating Cn2 Over Snow And Sea Ice From Meteorological Quantities. *Journal of the Optical Society of America*, *5*(4), 481–495. https://doi.org/10.1117/12.945784

Andreas, E. L. (1989). Two-Wavelength Method of Measuring Path-Averaged Turbulent Surface Heat Fluxes. *Journal of Atmospheric and Oceanic Technology*, *6*(1), 280–292. https://doi.org/10.1175/1520-0426(1990)007<0801:twmomp>2.0.co;2

Balsamo, G., Pappenberger, F., Dutra, E., Viterbo, P., & van den Hurk, B. (2011). A revised land hydrology in the ECMWF model: A step towards daily water flux prediction in a fully-closed water cycle. *Hydrological Processes*, *25*(7), 1046–1054. https://doi.org/10.1002/hyp.7808

Beljaars, A. C., & Bosveld, F. C. (1997). Cabauw data for the validation of land surface parameterization schemes. *Journal of Climate*, *10*(6), 1172–1193. https://doi.org/10.1175/1520-0442(1997)010<1172:CDFTVO>2.0.CO;2

Beyrich, F., De Bruin, H. A., Meijninger, W. M., Schipper, J. W., & Lohse, H. (2002). Results from one-year continuous operation of a large aperture scintillometer over a heterogeneous land surface. *Boundary-Layer Meteorology*, *105*(1), 85–97. https://doi.org/10.1023/A:1019640014027

Beyrich, F., Kouznetsov, R. D., Leps, J. P., Lüdi, A., Meijninger, W. M., & Weisensee, U. (2005). Structure parameters for temperature and humidity from simultaneous eddy-covariance and scintillometer measurements. *Meteorologische Zeitschrift*, *14*(5), 641–649. https://doi.org/10.1127/0941-2948/2005/0064

Braam, M. (2014). *Aspects of Atmospheric Turbulence related to Scintillometry* (Doctoral dissertation). Wagening University and Research.

Braam, M., Bosveld, F. C., & Moene, A. F. (2012). On Monin-Obukhov Scaling in and Above the Atmospheric Surface Layer: The Complexities of Elevated Scintillometer Measurements. *Boundary-Layer Meteorology*, *144*(2), 157–177. https://doi.org/10.1007/s10546-012-9716-7

Brunsell, N. A., Ham, J. M., & Arnold, K. A. (2011). Validating remotely sensed land surface fluxes in heterogeneous terrain with large aperture scintillometry. *International Journal of Remote Sensing*, *32*(21), 6295–6314. https://doi.org/10.1080/01431161.2010.508058

Cheng, Y., Sayde, C., Li, Q., Basara, J., Selker, J., Tanner, E., & Gentine, P. (2017). Failure of Taylor's hypothesis in the atmospheric surface layer and its correction for eddy-covariance measurements. *Geophysical Research Letters*, *44*(9), 4287–4295. https://doi.org/10.1002/2017GL073499

de Bruin, H. A. R., Nieveen, J. P., de Wekker, S. F. J., & Heusinkveld, B. G. (1996). Large aparture scintillometry over a 4.8 km path for measuring areally-average sensible heat flux; a case study. *Proc. 22nd Conf. on Agricultural & Forest Meteorology, Atlanta, Georgia, USA*, 153–156.

Esters, L., Rutgersson, A., Nilsson, E., & Sahlée, E. (2020). Non-local Impacts on Eddy-Covariance Air–Lake CO 2 Fluxes. *Boundary-Layer Meteorology*, *178*(2), 283–300. https://doi.org/10.1007/s10546-020-00565-2

Evans, J. G., McNeil, D. D., Finch, J. W., Murray, T., Harding, R. J., Ward, H. C., & Verhoef, A. (2012). Determination of turbulent heat fluxes using a large aperture scintillometer over undulating mixed agricultural terrain. *Agricultural and Forest Meteorology*, *166-167*, 221–233. https://doi.org/10.1016/j.agrformet.2012.07.010

Foken, T. (2008). The energy balance closure problem: An overview. *Ecological Applications*, *18*(6), 1351–1367. https://doi.org/10.1890/06-0922.1

George, W. K. (2010). Lectures in Turbulence for the 21st Century. *Department of Applied Mechanics Chalmers University of Technology Gothenburg, Sweden*, (January), 303.

Gibbs, J. A., & Fedorovich, E. (2020). On the Evaluation of the Proportionality Coefficient between the Turbulence Temperature Spectrum and Structure Parameter. *Journal of the Atmospheric Sciences*, *77*(8), 2761–2763. https://doi.org/10.1175/JAS-D-19-0344.1

Hartogensis, O. K. (2006). *Exploring Scintillometry in the Stable Atmospheric Surface Layer.* (Doctoral dissertation). Wageningen University and Research. https://doi.org/121762

Hartogensis, O. K., Watts, C., Rodriguez, J.-C., & De Bruin, H. A. (2003). Derivation of an Effective Height for Scintillometers: La Poza Experi-

ment in Northwest Mexico. *American Meteorological Society*, *4*(5), 915–928.

Hill, R. J. (1992). Review of optical scintillation methods of measuring the refractive-index spectrum, inner scale and surface fluxes. *Waves in random media*, *2*(3), 179–201.

Hill, R. J. (1997). Algorithms for obtaining atmospheric surface-layer fluxes from scintillation measurements. *Journal of Atmospheric and Oceanic Technology*, *14*(3), 456–467. https://doi.org/10.1175/1520-0426(1997)014<0456:AFOASL>2.0.CO;2

Hill, R. J., Clifford, S., & Lawrence, R. (1980). Refractive index and absorption fluctuations in the infrared caused by temperature, humidity, and pressure fluctuations. *Journal of the Optical Society of America*, *70*(10), 1192–1205.

Holtslag, A., & De Bruin, H. (1988). Applied modeling of the Nighttime Surface Energy Balance over Land. *Journal of Applied Meteorology*, *27*, 689–704.

Kanda, M., Inagaki, A., Letzel, M. O., Raasch, S., & Watanabe, T. (2004). Les study of the energy imbalance problem with eddy covariance fluxes. *Boundary-Layer Meteorology*, *110*(3), 381–404. https://doi.org/10.1023/B:BOUN.0000007225.45548.7a

Kochendorfer, J., Meyers, T. P., Frank, J., Massman, W. J., & Heuer, M. W. (2012). How well can we measure the vertical wind speed? Implications for fluxes of energy and mass. *Boundary-Layer Meteorology*, *145*(2), 383–398. https://doi.org/10.1007/s10546-012-9738-1

Kolmogorov, A. (1941). The local structure of turbulence in incompressible viscous fluid for very large Reynolds numbers. *Cr. Acad. Sci. URSS*, *30*(-), 301–305.

Kooijmans, L. M., & Hartogensis, O. K. (2016). Surface-Layer Similarity Functions for Dissipation Rate and Structure Parameters of Temperature and Humidity Based on Eleven Field Experiments. *Boundary-Layer Meteorology*, *160*(3), 501–527. https://doi.org/10.1007/s10546-016-0152-y

Liu, S. M., Xu, Z. W., Wang, W. Z., Jia, Z. Z., Zhu, M. J., Bai, J., & Wang, J. M. (2011). A comparison of eddy-covariance and large aperture scintillometer measurements with respect to the energy balance closure problem. *Hydrology and Earth System Sciences*, *15*(4), 1291–1306. https://doi.org/10.5194/hess-15-1291-2011

Lüdi, A., Beyrich, F., & Mätzler, C. (2005). Determination of the turbulent temperature-humidity correlation from scintillometric measurements. *Boundary-Layer Meteorology*, *117*(3), 525–550. https://doi.org/10.1007/s10546-005-1751-1

Maronga, B., Hartogensis, O. K., Raasch, S., & Beyrich, F. (2014). The Effect of Surface Heterogeneity on the Structure Parameters of Temperature and Specific Humidity: A Large-Eddy Simulation Case Study for the LITFASS-2003 Experiment. *Boundary-Layer Meteorology*, *153*(3), 441–470. https://doi.org/10.1007/s10546-014-9955-x

Meijninger, W. M. L., Beyrich, F., Lüdi, A., Kohsiek, W., & De Bruin, H. A. R. (2006). Scintillometer-based turbulent fluxes of sensible and latent heat

over a heterogeneous land surface - A contribution to LITFASS-2003. *Boundary-Layer Meteorology*, *121*(1), 89–110. https://doi.org/10.1007/s10546-005-9022-8

Meijninger, W. M. L., Hartogensis, O. K., Kohsiek, W., Hoedjes, J. C. B., Zuurbier, R. M., & De Bruin, H. A. R. (2002). Determination of Area-Averaged Sensible Heat Fluxes With a Large Aperture Scintillometer Over a Hetrogeneous Surface - Flevoland Field Experiment. *Boundary-Layer Meteorology*, *105*(1), 37–62. 10.1023/A:1019647732027%5Cnhttp://link.springer.com/10.1023/A:1019647732027

Moene, A. F., Meijninger, W. M. L., Hartogensis, O. K., Kohsiek, W., & De Bruin, H. A. R. (2004). *A review of the relationships describing the signal of a Large Aperture Scintillometer* (tech. rep.). http://www.met.wau.nl/internal_reports/

Monin, A., & Obukhov, A. (1954). Basic laws of turbulent mixing in the surface layer of the atmosphere. *Tr. Akad. Nauk SSSR Geophiz. Inst.*, *24*(151), 163–187.

Pasquariello, V., Hickel, S., & Adams, N. A. (2017). Unsteady effects of strong shock-wave/boundary-layer interaction at high Reynolds number. *Journal of Fluid Mechanics*, *823*, 617–657. https://doi.org/10.1017/jfm.2017.308

Pincus, R., Mlawer, E. J., & Delamere, J. S. (2019). Balancing Accuracy, Efficiency, and Flexibility in Radiation Calculations for Dynamical Models. *Journal of Advances in Modeling Earth Systems*, *11*(10), 3074–3089. https://doi.org/10.1029/2019MS001621

Richard, S., Colin, O., Vermorel, O., Benkenida, A., Angelberger, C., & Veynante, D. (2007). Towards large eddy simulation of combustion in spark ignition engines. *Proceedings of the Combustion Institute*, *31*(2), 3059–3066. https://doi.org/10.1016/j.proci.2006.07.086

Ruisdael Observatory. (2020). Cabauw experimental site for atmospheric research. https://ruisdael-observatory.nl/cesar-observatory/

Sagaut, P., & Deck, S. (2009). Large eddy simulation for aerodynamics: Status and perspectives. *Philosophical Transactions of the Royal Society A: Mathematical, Physical and Engineering Sciences*, *367*(1899), 2849–2860. https://doi.org/10.1098/rsta.2008.0269

Samain, B., Ferket, B. V., Defloor, W., & Pauwels, V. R. (2011). Estimation of catchment averaged sensible heat fluxes using a large aperture scintillometer. *Water Resources Research*, *47*(5), 1–17. https://doi.org/10.1029/2009WR009032

Samain, B., Simons, G. W., Voogt, M. P., Defloor, W., Bink, N. J., & Pauwels, V. R. (2012). Consistency between hydrological model, large aperture scintillometer and remote sensing based evapotranspiration estimates for a heterogeneous catchment. *Hydrology and Earth System Sciences*, *16*(7), 2095–2107. https://doi.org/10.5194/hess-16-2095-2012

Schalkwijk, J., Jonker, H. J., Siebesma, A. P., & Bosveld, F. C. (2015). A year-long large-eddy simulation of the weather over Cabauw: An overview.

Monthly Weather Review, *143*(3), 828–844. https://doi.org/10.1175/MWR-D-14-00293.1

Smagorinsky, J. (1963). General Circulation Experiments With The Primitive Equations. *Monthly Weather Review*, *91*(3), 99–164. https://doi.org/10.1126/science.23.592.714

Stiperski, I., Calaf, M., & Rotach, M. W. (2019). Scaling, Anisotropy, and Complexity in Near-Surface Atmospheric Turbulence. *Journal of Geophysical Research: Atmospheres*, *124*(3), 1428–1448. https://doi.org/10.1029/2018JD029383

Stoffer, R. (2018). *Revisiting Raw Data Processing of Combined Optical-Microwave Scintillometers* (Doctoral dissertation). Wageningen University.

Tatarskii, V. (1971). *The effect of the Turbulent Atmosphere on Wave Propagation*. Israel Program for Scientific Translations.

Upton, G. J., Holt, A. R., Cummings, R. J., Rahimi, A. R., & Goddard, J. W. (2005). Microwave links: The future for urban rainfall measurement? *Atmospheric Research*, *77*(1-4 SPEC. ISS.), 300–312. https://doi.org/10.1016/j.atmosres.2004.10.009

van de Boer, A. (2015). *Atmospheric turbulence over crops: confronting theories with observations*. (Doctoral dissertation). Wageningen. http://search.ebscohost.com/login.aspx?direct=true&db=lbh&AN=20153095167&site=ehost-live

Van Dinther, D., Hartogensis, O. K., & Moene, A. F. (2013). Crosswinds from a single-aperture scintillometer using spectral techniques. *Journal of Atmospheric and Oceanic Technology*, *30*(1), 3–21. https://doi.org/10.1175/JTECH-D-12-00069.1

Van Heerwaarden, C. C., Van Stratum, B. J., Heus, T., Gibbs, J. A., Fedorovich, E., & Mellado, J. P. (2017). MicroHH 1.0: A computational fluid dynamics code for direct numerical simulation and large-eddy simulation of atmospheric boundary layer flows. *Geoscientific Model Development*, *10*(8), 3145–3165. https://doi.org/10.5194/gmd-10-3145-2017

Vilà-Guerau De Arellano, J., Ney, P., Hartogensis, O., De Boer, H., Van Diepen, K., Emin, D., De Groot, G., Klosterhalfen, A., Langensiepen, M., Matveeva, M., Miranda-García, G., F. Moene, A., Rascher, U., Röckmann, T., Adnew, G., Brüggemann, N., Rothfuss, Y., & Graf, A. (2020). CloudRoots: Integration of advanced instrumental techniques and process modelling of sub-hourly and sub-kilometre land-Atmosphere interactions. *Biogeosciences*, *17*(17), 4375–4404. https://doi.org/10.5194/bg-17-4375-2020

Wang, T., Ochs, G., & Clifford, S. (1978). A saturation-resistant optical scintillometer to measure Cn2. *Journal of the Optical Society of America*, *68*(3), 334–338.

Ward, H. C., Evans, J. G., & Grimmond, C. S. (2015). Infrared and millimetre-wave scintillometry in the suburban environment -Part 2: Large-area sensible and latent heat fluxes. *Atmospheric Measurement Techniques*, *8*(3), 1407–1424. https://doi.org/10.5194/amt-8-1407-2015

Ward, H. C., Evans, J. G., Grimmond, C. S., & Bradford, J. (2015). Infrared and millimetre-wave scintillometry in the suburban environment-Part

1: Structure parameters. *Atmospheric Measurement Techniques*, *8*(3), 1385–1405. https://doi.org/10.5194/amt-8-1385-2015

Ward, H. C., Evans, J. G., Hartogensis, O. K., Moene, A. F., De Bruin, H. A., & Grimmond, C. S. (2013). A critical revision of the estimation of the latent heat flux from two-wavelength scintillometry. *Quarterly Journal of the Royal Meteorological Society*, *139*(676), 1912–1922. https://doi.org/10.1002/qj.2076

Ward, H. C. (2017). Scintillometry in urban and complex environments: A review. *Measurement Science and Technology*, *28*(6). https://doi.org/10.1088/1361-6501/aa5e85

Wesely, M. L. (1976). A Comparison of Two Optical Methods for Measuring Line Averages of Thermal Exchanges Above Warm Water Surfaces. *Journal of Applied Meteorology*, *15*(11), 1177–1188. https://doi.org/10.4135/9781412963893.n25

Wesson, K. H., Katul, G. G., & Siqueira, M. (2003). Quantifying organization of atmospheric turbulent eddy motion using nonlinear time series analysis. *Boundary-Layer Meteorology*, *106*(3), 507–525. https://doi.org/10.1023/A:1021226722588

Wicker, L. J., & Skamarock, W. C. (2002). Time-splitting methods for elastic models using forward time schemes. *Monthly Weather Review*, *130*(8), 2088–2097. https://doi.org/10.1175/1520-0493(2002)130<2088:TSMFEM>2.0.CO;2

Xin, L., Fei, H., & Gang, L. (2001). Characteristics of chaotic attractors in atmospheric boundary-layer turbulence. *Boundary-Layer Meteorology*, *99*(2), 335–345. https://doi.org/10.1023/A:1018940512240

9 Appendices

A Angular eddy hypothesis

In the turbulent atmosphere, buoyant eddies organize themselves in turbulent organized structures (Kanda et al., 2004; Wesson et al., 2003). We imagine this process as a suction effect, where the acceleration of an upwards eddy sucks other eddies into the slight under pressure it leaves behind. Here, other upward moving (i.e. warm and wet) eddies are more likely to be sucked in as the upward movement is in line with their momentum. Crucially, the eddies which get sucked in are likely to exert a horizontal movement (see figure 36). This is because the surface prevents eddies from rising straight up because otherwise an even more significant under pressure would be created at the surface (Here, we expect surface roughness causes extra resistance to compensating horizontal movements.). To equalize pressure, downward moving eddies can be expected move in the opposite horizontal direction, casing the net turbulent flux to get an angle (α). It is important to note that during advection, eddies get a horizontal motion too. However, both the ascending and descending eddies move in the same horizontal direction (see figure 36). In principle this shouldn't result in a horizontal flux if it wasn't for the fact that u and X will gain some cross-correlation through mechanical shear as it results in $\overline{u'w'} < 0$ (as long as there is a vertical exchange of X). Also, the fact that $u >> w$, generates a larger relative error in $\overline{u'X'}$ then in $\overline{w'X'}$. If our hypothesis is correct, there will also be an additional non-artificial part to $\overline{u'X'}$. Note that the process we describe could exist at several scales superimposed on each other, where larger and larger eddies are merged. Thus, while conventional (large) turbulent organized structures are known for their stationary in space, the process we describe might also occur at smaller scales with large temporal and spacial variability. Consequently, in a 10-minute interval measured with an EC-system, we might find that $\overline{w} = 0$ when the horizontal plain is parallel to the surface, while the angle of the fluxes (α) has varied between -20° and +20° (figure 36).

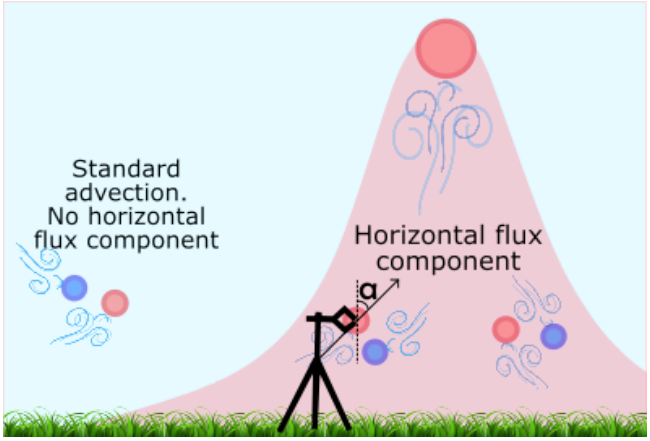

Figure 36: Conceptual image of 'Angular eddy hypothesis', where a part of the turbulent flux is transferred in the horizontal direction.

If this phenomenon occurred, it would explain the systematic underestimation of turbulent fluxes by Eddy Covariance. Recent work by Stiperski et al. (2019) does proof that $\overline{u'X'}$ contains important information which might help solve MOST non-universality. We hypothesise that $\overline{u'X'}$ might also contains the key to unlock the energy balance closure problem.

B Additional figures & tables

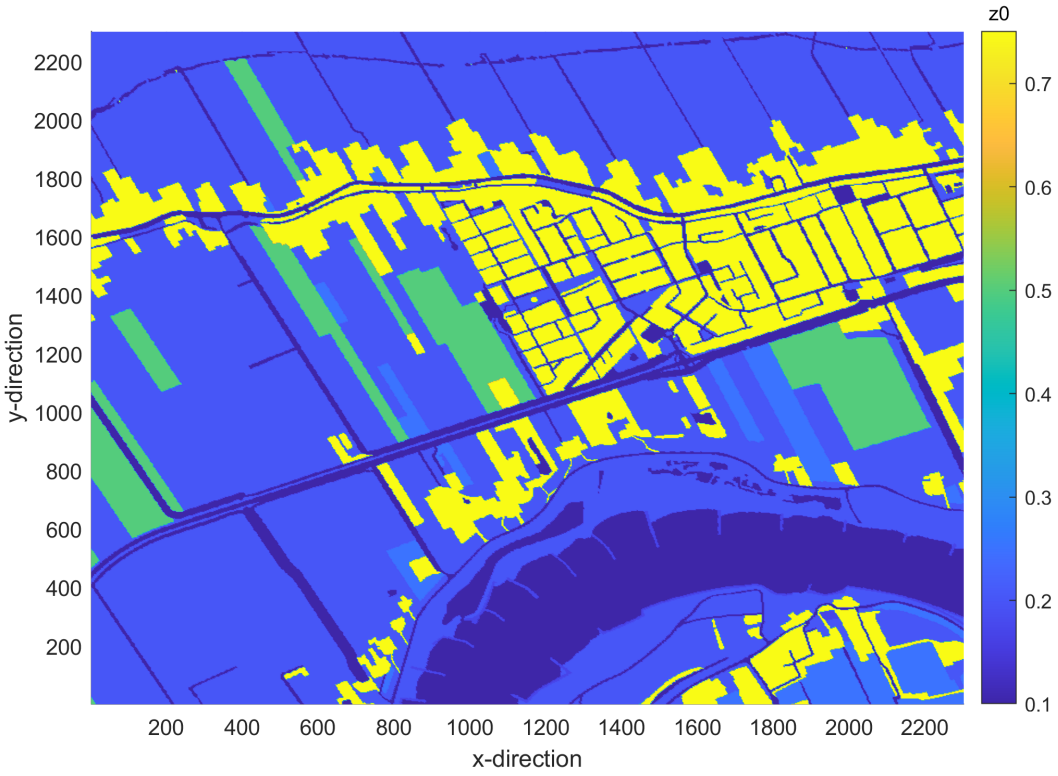

Figure 37: Land used dependant z_0 at the surface of the LES.

Table 6: MOST coefficients determined by our WD dependent MOST optimization scheme. Here, z_0 was also WD dependent z_0. Colors indicate similarity to margins around general coefficients by Kooijmans and Hartogensis. Green; within margins, yellow; near margins, and red; not near margins.

Optimized MOST coefficients	50-150		150-320		320-50	
Unstable conditions ($\zeta < 0$)	$f_{C_T^2}$	$f_{C_q^2}$	$f_{C_T^2}$	$f_{C_q^2}$	$f_{C_T^2}$	$f_{C_q^2}$
c_1	4.8	4.0	6.5	6.0	4.0	4.0
c_2	4.2	13.0	8.2	9.4	4.5	7.1
Stable conditions ($\zeta > 0$)	$f_{C_T^2}$	$f_{C_q^2}$	$f_{C_T^2}$	$f_{C_q^2}$	$f_{C_T^2}$	$f_{C_q^2}$
c_1	4.0	4.3	5.0	6.0	5.6	4.0
c_2	0.0	0.0	0.0	2.1	4.0	0.0

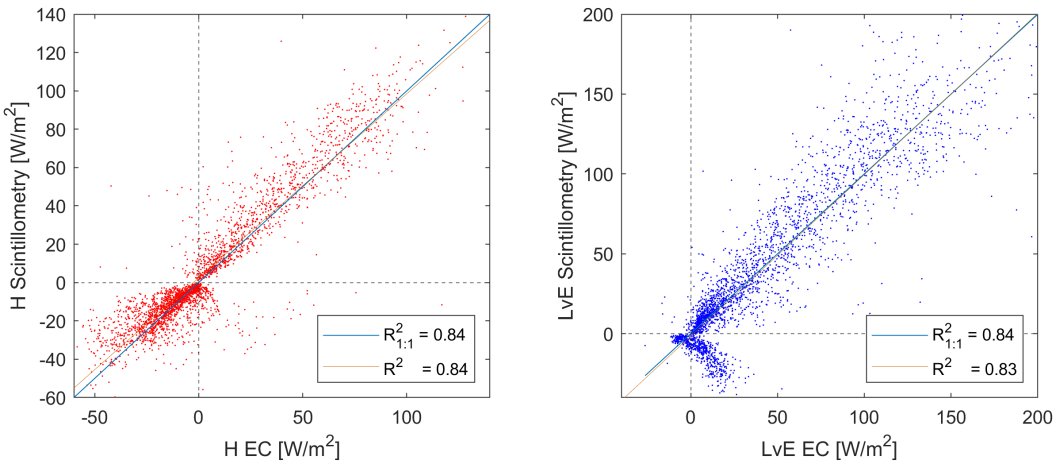

Figure 38: Comparison of the most accurate scintillometer fluxes to those from EC. Scintillometer fluxes were calculated with: WD dependant MOST coefficients (table 6) z_0 from EC data.

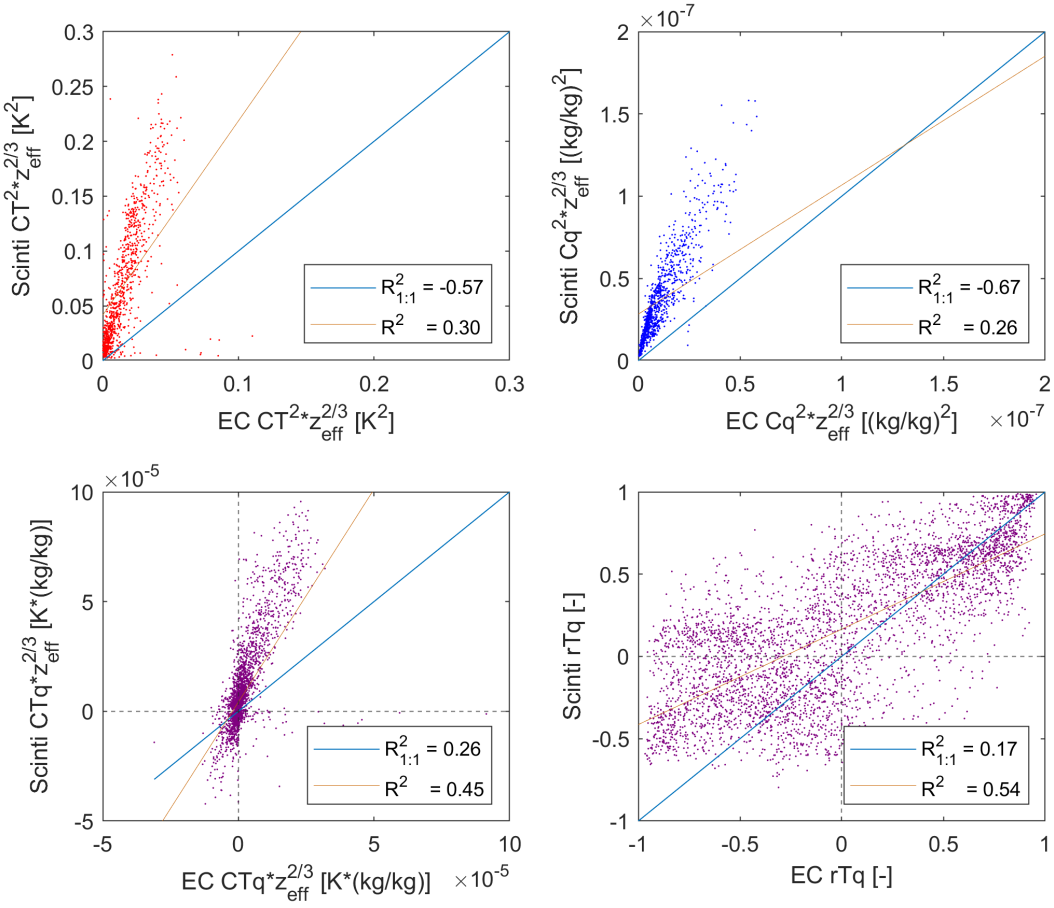

Figure 39: Comparison between EC and scintillometry on structure parameter level. Here the EC structure parameters were calculated with spectra.

C Surface layer meteorology

In essence, meteorology is nothing but the transport of moisture and heat from one place to another to compensate for differential solar irradiation. It is therefore important to understand the mechanism by which this solar radiation is converted into heat and moisture fluxes. Since this conversion primarily occurs at the earth's surface, surface layer meteorology is the field responsible for advancing this understanding. The knowledge gained within this field by taking (relatively) direct in situ measurements of the sensible and latent heat fluxes (H and LvE respectively) and the rest of the terms in the energy balance is of direct help in many hydro-meteorological applications. For example; flood warning systems that need to know the evapotranspiration in their catchments (Samain et al., 2011) or numerical weather prediction models and remote sensing techniques that must be validated or need to be parameterized. (Beyrich et al., 2002; Brunsell et al., 2011; Samain et al., 2012). It is for these reasons that advances in surface layer meteorology are crucial.

The main obstacle in surface layer meteorology is the turbulent - and thus inherently unpredictable - nature of the main vertical transport mechanism of heat and moisture. It occurs because air parcels that get heated and moistened at the earth's surface (during daytime) get lighter then their colder and dryer counterparts higher in the atmosphere. As a consequence, the light air parcels (eddies) rise and the heavy eddies fall, causing the turbulent mixing that is observed (buoyancy). After their creation, the turbulent eddies interact, and break up into smaller and smaller eddies as first described by Kolmogorov (1941). The eddies in this stage are in the so-called inertial sub-range, which is associated with a specific range of eddy scales. After getting smaller than the inner scale of turbulence, the momentum gets dissipated as heat through viscosity. This process continues as long as the surface has net energy left over to heat air and evaporate water. During daytime this is nearly always the case, resulting in the so-called convective boundary layer (CBL) which is a well-mixed layer which can grow up to several kilometres height.

D Brief history of Scintillometry

In 1976, scintillometry was already applied with the goal of determining H and LvE fluxes (Wesely, 1976). However, this was at a short range. Also, it only had a wavelength in the optical range of the electromagnetic spectrum, making it a lot more sensitive to H then to LvE. Since then, some crucial advances have been made which have moved the understanding of scintillometry along. Importantly, Large Aperture Scintillometers (LAS) became available for optical wavelengths, which allowed for measurements over longer range ($\sim$5Km, see e.g. de Bruin et al., 1996), thus aiding the spatial averaging. Furthermore, the idea of using two scintillometers of different λ's to determine H and LvE - in which λ_1 would be sensitive to variations in T and λ_2 to variations in q - was proposed by Andreas in 1989. He suggested to use a near optical/infrared wavelength

for λ_1 and a millimetre/microwave wavelength for λ_2. Hill worked this out into the so-called 'two-wavelength' or 'Hill' method that is now commonly used in scintillometry (Hill, 1997). Lüdi made a variation on this method in Lüdi et al., 2005 by calculating an additional cross-correlation term from the two signals. This removed the need for an assumed correlation between the fluctuations in T and q ($r_T q$) which is a major weakness in the 'Hill' method[28]. Since these theoretical derivations, the measurement equipment has become better and more affordable, with wider availability of Microwave Scintillometers (MWS) being the latest trend. Also, smaller and larger theoretical updates have continued (see e.g. Ward et al., 2013), with the most recent leap being made by Kooijmans in 2016. They merged data from 11 different studies to find MOST functions[29] that significantly reduced the error margins in the output fluxes which should unify and equalize future scintillometer studies (Kooijmans and Hartogensis, 2016). To summarize, although the principle of scintillometry is not brand new, it is still actively under development (well portrayed in Ward, 2017 figure 3).

[28] See section 2.2.4

[29] MOST = Monin Obukhov Similarity Theory, see section 2.2.5